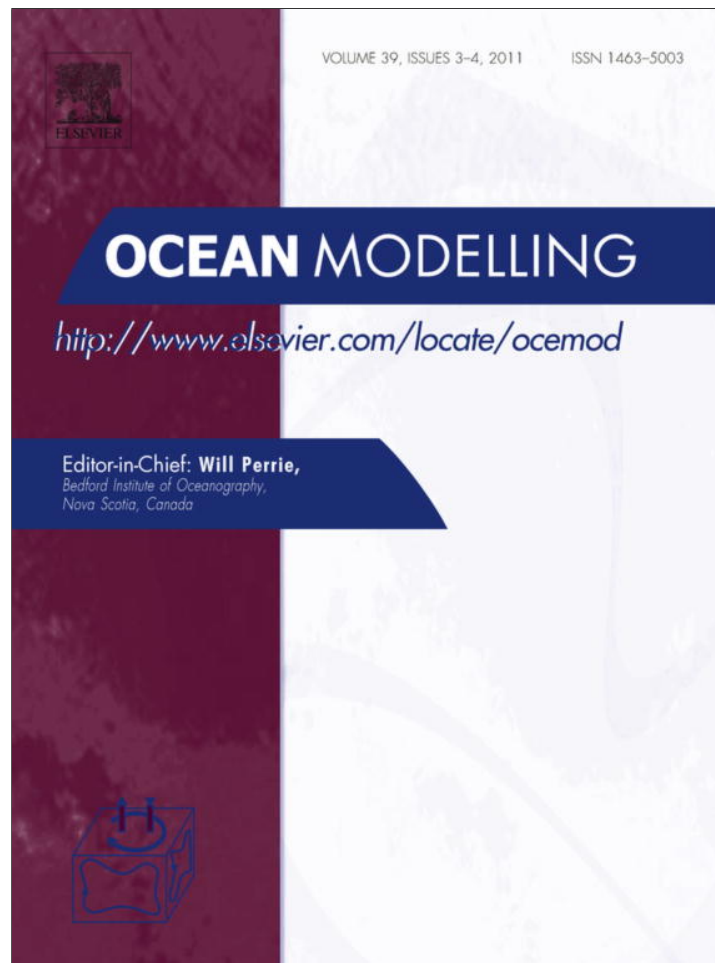


Provided for non-commercial research and education use.  
Not for reproduction, distribution or commercial use.



This article appeared in a journal published by Elsevier. The attached copy is furnished to the author for internal non-commercial research and education use, including for instruction at the authors institution and sharing with colleagues.

Other uses, including reproduction and distribution, or selling or licensing copies, or posting to personal, institutional or third party websites are prohibited.

In most cases authors are permitted to post their version of the article (e.g. in Word or Tex form) to their personal website or institutional repository. Authors requiring further information regarding Elsevier's archiving and manuscript policies are encouraged to visit:

<http://www.elsevier.com/copyright>



Contents lists available at ScienceDirect

## Ocean Modelling

journal homepage: [www.elsevier.com/locate/ocemod](http://www.elsevier.com/locate/ocemod)

## Large eddy simulations of mixed layer instabilities and sampling strategies

Tamay M. Özgökmen<sup>a,\*</sup>, Andrew C. Poje<sup>b</sup>, Paul F. Fischer<sup>c</sup>, Angelique C. Haza<sup>a</sup><sup>a</sup> RSMAS, University of Miami, Miami, FL, United States<sup>b</sup> Department of Mathematics, College of Staten Island, Staten Island, NY, United States<sup>c</sup> Math. and Computer Sci. Division, Argonne National Laboratory, Argonne, IL, United States

## ARTICLE INFO

## Article history:

Received 24 January 2011

Received in revised form 15 May 2011

Accepted 18 May 2011

Available online 26 May 2011

## Keywords:

Submesoscale

Lagrangian sampling

Tracers

## ABSTRACT

Recognizing the potential role played by submesoscale processes in both the energy cascade in the ocean and biogeochemical transport, we conduct a series of large eddy simulations of isolated mixed layer instabilities. The primary objective is to generate freely evolving velocity and density fields representative of submesoscale flows and then use these to examine potential observational sampling strategies. Mixed layer instabilities are explored in two parameter regimes: a strongly-stratified regime which results in a system with surface-intensified eddies and high vertical shear, and a weakly-stratified regime exhibiting weaker, smaller scale eddies that penetrate across the entire domain depth as Taylor columns. Analysis of a variety of mixing measures derived from both particle and tracer based sampling strategies indicates the differing importance of vertical processes in the two flow regimes.

© 2011 Elsevier Ltd. All rights reserved.

## 1. Introduction

Investigation of the production, maintenance and dynamics of submesoscale ( $O(100)$  m to  $O(10)$  km) flows in the ocean has been an area of active research for several decades (McWilliams, 1985; Thomas et al., 2008). Developments in satellite remote sensing technology, computer power, numerical and data assimilation methods have been such that ocean general circulation models (OGCMs) and remote-sensing platforms now arguably allow for both the routine observation and forecasting of the main turbulent features of the ocean circulation, namely the mesoscale eddies and jets (Chassignet et al., 2006; Capet et al., 2008; Martin et al., 2009). Understanding the dynamics of coherent turbulent features at the submesoscale and accurately parameterizing their effects on larger scale motions is a natural next step which is critically important for a number of reasons.

## 1.1. Dynamical impacts

First, as emphasized by the comprehensive study by Wunsch and Ferrari (2004), there are fundamental questions about the energetics of the ocean general circulation. Of particular interest are the pathways to dissipation. Given the fact that oceanic mesoscale features generated by barotropic and baroclinic instabilities of the general circulation have a scale on the order of the Rossby radius of deformation,  $O(10^4)$  m, while the ultimate dissipation of energy by molecular viscosity takes place at scales of motion of  $O(10^{-2})$  m, submesoscale motions necessarily act to mediate the

overall energy cascade. The behavior of flows in geostrophic (or gradient wind) balance in the high-aspect ratio of ocean domains tends to be analogous to two-dimensional (2D) turbulence where the energy cascade is primarily toward larger scales. This creates a conundrum about how motions at mesoscales, submesoscales, and smaller scales coexist and interact (Müller et al., 2005) and, in particular, how the forward cascade of energy takes place (McWilliams, 2008). The relative role of organized, submesoscale motions produced by instabilities and other dynamic processes such as internal gravity waves and topographic interactions in the ultimate dissipation of energy remains unclear (Wunsch and Ferrari, 2004).

In addition to being critical for constructing a fundamental picture of the overall ocean energy balance, submesoscale flows have direct implications for practical problems. For instance, naval ships and submerged equipment such as submarines are subject to currents at the submesoscale range, the fate of coastal discharges could be influenced by such flows, and high vertical velocities in submesoscale fronts and filaments (Mahadevan and Tandon, 2006) are likely to play an important role in the transport of biogeochemical tracers (Klein and Lapeyre, 2009). As OGCMs are increasingly used to predict and quantify smaller scale transport questions, the need to ultimately incorporate accurate representations of submesoscale flows also increases.

A particular class of submesoscale flows is thought to occur in the surface mixed layer. External forcings generated by storms and heating events create fronts of lateral buoyancy gradients, which are then subject to adjustment by converting the available potential energy in the frontal structure to kinetic energy (Tandon and Garrett, 1994). Recent numerical studies indicate that this adjustment takes the form of baroclinic instabilities associated

\* Corresponding author. Tel.: +1 305 421 4053.

E-mail address: [tozgekmen@rsmas.miami.edu](mailto:tozgekmen@rsmas.miami.edu) (T.M. Özgökmen).

with the stratification of the mixed layer fronts. So-called mixed layer instabilities create coherent eddies typically an order of magnitude smaller ( $O(10^3)$  m) than the radius of deformation associated with the mesoscale and are essential contributors to mixed layer restratification (Boccaletti et al., 2007; Fox-Kemper et al., 2008; Mahadevan et al., 2010). As such, this type of flow provides a clear mechanism for the direct generation of submesoscale fields. While such flows coexist and interact with existing mesoscale features in the ocean, our goal here is to investigate their isolated dynamics before tackling the grand challenge of multi-scale interactions.

### 1.2. Observational methods

The complexity of submesoscale flows implied above leads to the natural question of how to observe and sample these flows in the real ocean (Badin et al., in press). The observation of such submesoscale phenomena through traditional ocean observing systems is challenging because the spatial and temporal scales involved fall in between the scales for which many traditional instruments have been optimized. For instance, multiple ships are likely to be required in order provide synoptic coverage of the flow field using traditional instruments, such as CDTs (conductivity, depth, temperature sensor) or ADCPs (acoustic Doppler current profiler). Newly emerging instruments such as gliders can be guided to generate detailed profiles of these features but gliders are difficult to navigate when current speeds exceed  $0.25 \text{ m s}^{-1}$  (Webb et al., 2001). This can pose challenges near strong fronts, or if submesoscale features are imbedded in strong mesoscale eddies thus possibly limiting their use for synoptic sampling of rapidly-evolving fields. Satellite remote sensing is promising in that new altimeters with a spatial resolution of 1 km are likely to be deployed in the future (Peter Minnett, personal communication, 2010). Nevertheless, interpretation of the signal and how it relates to the velocity field are challenges yet to be resolved. For instance, when higher resolution products become available, errors associated with the Earth's gravity anomalies and waves can become comparable to the ocean's surface topography signal created by submesoscale flows, and geostrophic approximation used in estimating currents may not be valid. Ocean color sensors reveal significant detail ([http://oceancolor.gsfc.nasa.gov/cgi/image\\_archive.cgi?c=CHLOROPHYLL](http://oceancolor.gsfc.nasa.gov/cgi/image_archive.cgi?c=CHLOROPHYLL)). Nevertheless, they only detect chlorophyll, which is mostly limited to coastal regions. It is also not clear how to interpret this signal and relate to primary variables of interest (e.g., velocity and density fields), given that it represents a complex combination of depth-averaged distribution of a quasi-passive scalar field. Radars are very useful (Steward and Joy, 1974; Shay et al., 1998a, 2001; Paduan and Rosenfeld, 1996; Kaplan et al., 2005; Paduan et al., 2006; Shay et al., 2007), but they are constrained to coastal regions and surface flows presently. Two other classes of instruments seem to offer the promise of 2D + 1 (time evolution of horizontal fields), and even 3D + 1 sampling. The first is drifters and floats, which have a long history of development (Davis, 1991; Poulain, 1999). There are various forms of drifting instruments. RAFOS floats use acoustic tracking (Rossby, 2007). Isopycnal and isobaric operations of such floats are ideally suited for sampling mesoscale circulation features away from the surface and the bottom of the ocean. Profiling floats (PALACE, ARGO) are used to map out the hydrography. These floats are programmed to follow a certain depth profile, and surface regularly to report their positions via satellite communication. Due to vertical shear encountered during their vertical movement, these instruments pose challenges for retrieving velocity information. SVP drifters are drogued typically at 15 m below the surface, and are widely used to measure near-surface currents representative of mixed layers. Communication with Argos satellite system allows

position fixes with an uncertainty of about 150–1000 m (Lumpkin and Pazos, 2007). Low-cost CODE surface drifters can be fitted with GPS receivers, which allow position accuracy down to 10 m (Poulain, 1999). Lagrangian floats (D'Asaro, 2003) are designed to track the motion of water parcels in 3D. In this sense, they are ideally suited for mixed layer sampling. Vertical velocities are inferred from the rate of pressure change, while horizontal positions can be tracked acoustically. These floats can also accurately track the 3D motion along an isopycnal. The addition of sensors measuring shear and a variety biological and chemical quantities, allows detailed studies of the evolution of these quantities from a Lagrangian and/or isopycnal viewpoint. Any decrease in the cost of the drifting instruments is likely to pave the way for their deployment in large clusters.

The second class of instrumentation of great interest here is the airborne lidar, which allows for a near-synoptic and 3D mapping of fluorescent dye in the upper ocean (Sundermeyer et al., 2007). Further development of this instrument is likely to make significant advances in upper ocean observations using tracers. Perhaps most importantly, both techniques are Lagrangian, namely they naturally follow the fluid motion. When resources are limited, this could be an important advantage over fixed-grid approaches for rapidly-deforming submesoscale fields.

### 1.3. Goals and structure

Our main goals in this study are as follows:

- (a) To generate mixed layer instabilities numerically, in the absence winds and modeled/resolved interactions with mesoscale features, as an idealized example of isolated submesoscale flow fields in the ocean, and to investigate the mixing produced by dynamically consistent submesoscale features.
- (b) To examine the efficiency and accuracy of potential Lagrangian sampling platforms, specifically by comparing and contrasting drifter and tracer based observations.

The paper is organized as follows: The modeling approach is introduced Section 2. The model configuration and the parameters of the numerical experiments are outlined in Section 3. A short description of the fields is provided in Section 4. Results from sampling strategies are presented in Section 5. Finally, the principal findings and future directions are summarized in Section 6.

## 2. Numerical model

This numerical study is conducted using Nek5000, which integrates Boussinesq equations based on the spectral element method (Patera, 1984; Maday and Patera, 1989; Fischer, 1997). Nek5000 has been previously used in idealized studies of gravity currents (Özgökmen et al., 2004a,b; Özgökmen et al., 2006; Özgökmen and Fischer, 2008) and these results have formed the basis of refined parameterizations of gravity current mixing for an ocean general circulation model (Chang et al., 2005; Xu et al., 2006). Nek5000 was also employed in studies of exchange flows (Ilicak et al., 2009) and the development of subgrid-scale (SGS) models in large eddy simulations (LES) of mixing in stratified flows (Özgökmen et al., 2007; Özgökmen et al., 2009a,b).

Nek5000 is configured to integrate the non-dimensionalized Boussinesq equations:

$$\begin{cases} \frac{D\bar{\mathbf{u}}}{Dt} = Ro_H^{-1} \hat{\mathbf{z}} \times \bar{\mathbf{u}} - \nabla \bar{p} - Fr^{-2} \bar{\rho}' \hat{\mathbf{z}} + Re^{-1} \nabla^2 \bar{\mathbf{u}} - \nabla \cdot \boldsymbol{\tau}, \\ \nabla \cdot \bar{\mathbf{u}} = 0, \\ \frac{D\bar{\rho}'}{Dt} = Pe^{-1} \nabla^2 \bar{\rho}' - \nabla \cdot \boldsymbol{\sigma}. \end{cases} \quad (1)$$

The overbar denotes quantities which vary on the resolved scales of the LES simulation. In particular,  $\bar{\rho}'$  is the resolved-scale density perturbation field in the Boussinesq approximation,  $\rho = \rho_0 + \rho'$ , with  $\rho' \ll \rho_0$ , where  $\rho_0$  is the fluid density.

The non-dimensional parameters in the simulation are the Reynolds number  $Re = U_0 H_0 / \nu$ , the Peclet number  $U_0 H_0 / \kappa$ , the Froude number  $Fr = U_0 / (NH_0)$ , and the vertical Rossby number  $Ro_H = U_0 / (fH_0) = aRo$ , where  $Ro = U_0 / (fL)$  is the Rossby number and  $a = L/H_0$  the ratio of horizontal and vertical domain sizes.  $U_0$  is the flow speed scale,  $H_0$  the total fluid depth,  $\nu$  is the kinematic viscosity,  $\kappa$  is the molecular diffusivity,  $g$  is the gravitational acceleration,  $N$  is the buoyancy frequency,  $f$  is the Coriolis frequency and  $\hat{z}$  is the unit vector in the vertical direction.

In (1),  $\frac{D}{Dt} := \frac{\partial}{\partial t} + \bar{\mathbf{u}} \cdot \nabla$  is the material derivative and the variables are considered to be spatially filtered velocity  $\bar{\mathbf{u}} = (\bar{u}, \bar{v}, \bar{w})$ , pressure  $\bar{p}$ , and density perturbation  $\bar{\rho}'$ . The subgrid scale terms  $\boldsymbol{\tau} = \bar{\mathbf{u}}\bar{\mathbf{u}} - \mathbf{u}\mathbf{u}$  and  $\boldsymbol{\sigma} = \bar{\mathbf{u}}\bar{\rho}' - \mathbf{u}\rho'$ , arise due to spatial filtering with LES. Here, we use the dynamic Smagorinsky SGS model for  $\boldsymbol{\tau}$  and  $\boldsymbol{\sigma} = 0$ . The reader is referred to Özgökmen et al. (2009a,b) for further details.

In addition to (1), two equations related to particle and tracer based sampling strategies are also solved using Nek5000. The first is the advection–diffusion equation for a passive scalar (tracer) field  $C$ :

$$\frac{DC}{Dt} = Pe^{-1} \nabla^2 C. \quad (2)$$

The other is the Lagrangian advection equation for passive, neutrally buoyant particles,

$$\frac{d\mathbf{x}}{dt} = \bar{\mathbf{u}}, \quad (3)$$

where  $\mathbf{x}$  represents the (3D or 2D) time dependent particle position.

### 3. Model setup and parameters

While one of the strengths of the spectral element method is geometrical flexibility, the assumption of an upper ocean flow away from complicated vertical or horizontal boundaries implies that the computational domain consists of a simple rectangular box. The primary length scale is taken as the total fluid depth  $H_0$  with a value on the order of a typical main thermocline,  $H_0 \approx 500$  m. The results are discussed using a combination of dimensional (indicated by primes) and nondimensional numbers. The dimensional domain depth is  $H' = HH_0 = 500$  m ( $H = 1$ ), and the domain width is taken equal to its length,  $L' = LH_0 = 10,000$  m ( $L = 20$ ). The boundary conditions are periodic in  $x$  direction, and consist of free-slip, insulated walls in the other ( $y = 0, y = L, z = 0, z = H$ ) directions.

The initial value problem we are interested in is the adjustment of a density front, possibly generated by a warming event, storm, buoyant outflow, or a wind-driven upwelling event. Such problems have received much interest recently (Mahadevan, 2006; Boccaletti et al., 2007; Thomas et al., 2008; Fox-Kemper et al., 2008). While the chosen initial condition is guided by an observation (i.e., Fig. 2b in Lee et al. (2009) collected during the AESOP – Assessing the Effects of Submesoscale Ocean Parameterizations – program in Monterey Bay), the idealized profile is given by:

$$\rho'(\mathbf{x}, 0) = \left[ 1 - 0.7 \frac{z}{H} \left( 1 + \frac{y}{L} \right)^{2.3} \right] \times \left[ 1 - \exp \left\{ - \left( \frac{y/L}{0.5 + 0.05 \cos(2\pi \frac{x}{L})} \right)^4 - \left( 5 \left( 1 - \frac{z}{H} \right) \right)^8 \right\} \right]. \quad (4)$$

Specifically, the profile represents a  $h_0 \approx 80$  m deep mixed layer and a 3 km wide front resting on a stably-stratified fluid (Fig. 1a). A symmetry-breaking, sinusoidal perturbation is superimposed in the lateral ( $x$ ) direction (Fig. 1b).

Integrations are started from rest and contain no forcing. Wind forcing is neglected here for reasons of dynamical simplicity and in order to limit the parameter space.

The domain is discretized using  $K_x = K_y = 32$  and  $K_z = 8$  ( $K = K_x K_y K_z = 8192$ ) elements in the horizontal and vertical directions, respectively. The horizontal elements have uniform spacing while those in the vertical are clustered near the surface in order to better resolve mixed layer instabilities (Fig. 1b). Most computations for the basic flow field and sampling strategies are conducted using  $\mathcal{N} = 8$ th order polynomials, but we have conducted higher resolution simulations with  $\mathcal{N} = 11$  and  $\mathcal{N} = 15$  as well. The mesh spacings are listed in Table 1.

The model parameters are selected as follows. As implied above, it is desirable to set  $Re$  as high as possible for oceanic flows so that the range of turbulent scales is dictated by resolved dynamics, as opposed to numerical viscosity. After some parameter experimentation, we set  $Re = 10^5$ . The reader is referred to Özgökmen et al. (2009b) for a recent effort to study the effects of  $Re$  on stratified

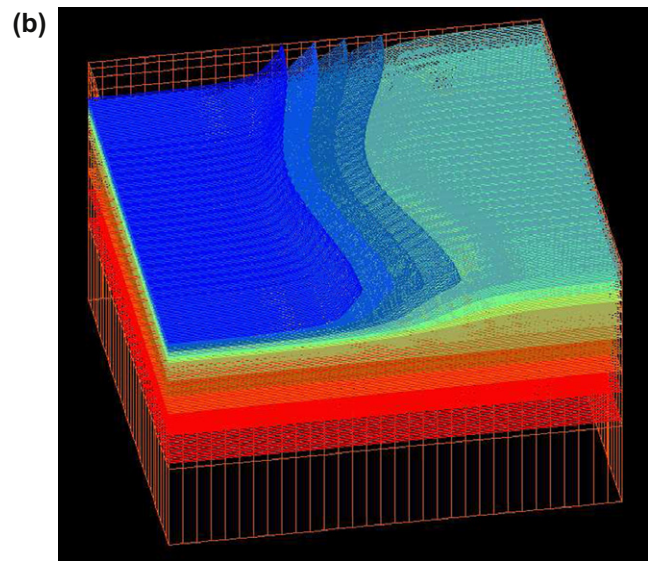
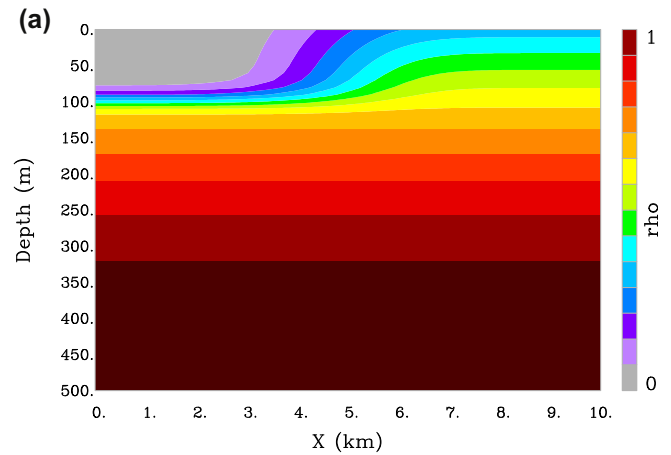


**Fig. 1.** Initial condition for the density perturbation field  $\bar{\rho}'(\mathbf{x}, t = 0)$ , (a) vertical cross section and (b) 3D view. In (b), the vertical axis is stretched 10-fold with respect to the realistic aspect ratio. The wire frame depicts the distribution of the elements.

**Table 1**

Table of the spatial resolutions used for the numerical simulations. The number of grid points is  $n = (K_x \mathcal{N} + 1)(K_y \mathcal{N} + 1)(K_z \mathcal{N} + 1)$ , where  $K_x = K_y = 32$ ,  $K_z = 8$ . The grid spacing within each element changes according to the distribution of GLL points that are clustered close to the inter-element boundaries to reduce Gibbs oscillations, where the maximum spacing is  $(\Delta x)_{\max} \approx \ell \frac{\pi}{2\mathcal{N}}$  and the minimum is  $(\Delta x)_{\min} \approx \ell \frac{5}{\mathcal{N}^2}$  for a given element length  $\ell$ . The vertical spacings are listed for the element closest to the upper boundary. The computation time for one model time step scales with  $K\mathcal{N}^4$ .

Exp.	$\mathcal{N}$	Spatial points $n$	$\Delta x = \Delta y$ min to max	$\Delta z$ min to max
standard	8	4,293,185	15–57 m	0.7–2.4 m
high-res1	11	11,090,201	9–43 m	0.4–1.8 m
high-res2	15	27,994,681	5–32 m	0.2–1.3 m

mixing. Next, we set  $Pe = 7 \times 10^5$  since their ratio is the Prandtl number  $Pr = Pe/Re = 7$ , which is consistent with that of heat and water.

Here, we consider two types of flows, characterized by a wide range of  $Fr$ . Strongly-stratified flows are represented by  $Fr = 0.1$ , while weakly-stratified flows are obtained by setting  $Fr = 1.0$ . While there must be surely flows that are characterized by  $Fr$  beyond and in between these values, it is assumed that these values are adequately far apart and representative of the oceanic range so that any sampling strategies can be meaningfully projected for practical applications in the field.

The final parameter  $Ro$  is set as follows. We aim for a parameter regime that provides us with a reasonable compromise between capturing the interaction of many turbulent features, or details of a single one, given the computational limitations. In other words, one can zoom into (out of) coherent structures by increasing (decreasing)  $Ro$ . The scale of the fastest growing modes  $\mathcal{R}$  in the mixed layer instability over a wide parameter regime falls in a narrow range of  $4 \leq \mathcal{R}/R_d \leq 6$  (Eldevik and Dysthe, 2002), where  $R_d = \sqrt{\frac{g}{\rho_0} \Delta \rho'_m h_0} / f$  is the radius of deformation in the mixed layer with  $\Delta \rho'_m$  being the density change across the surface front. Assuming  $\mathcal{R}/R_d \approx 5$  for simplicity, the size of mixed layer eddies within the horizontal extent of the domain can be estimated from  $\frac{\mathcal{R}}{L'} \approx 5 \frac{Ro}{Fr} \sqrt{\frac{\Delta \rho'_m}{\rho_0} \frac{h_0}{H_0}}$ . Substituting from Fig. 1a  $\Delta \rho'_m / \Delta \rho' \approx 0.3$  and  $h_0 / H_0 \approx 80/500$ , we get  $L' / \mathcal{R} \approx Fr / Ro$ . By setting  $Ro = 0.02$ , one obtains  $L' / \mathcal{R} \approx 5$  (or  $\mathcal{R} \approx 2$  km) with  $Fr = 0.1$  and  $L' / \mathcal{R} \approx 50$  (or  $\mathcal{R} \approx 0.2$  km) with  $Fr = 1.0$ . These features fall within the submesoscale range of 100 m to 10 km (Thomas et al., 2008).

The computations are conducted on 64–256 processors on Virginia Tech's systemX, as well as Linux and IBM-P5 clusters at the University of Miami. Most numerical experiments take a wall clock time of up to 1 week for obtaining the main fields, and 12–24 h for the Lagrangian and tracer sampling experiments.

#### 4. Description of the fields

Since the model is initialized from rest, the first step is to develop dynamically consistent velocity fields. These are obtained by first running on a very coarse grid with  $\mathcal{N} = 4$  so that the front can adjust geostrophically. During this spin-up phase the resolution is coarse enough so that mixed layer instabilities are not permitted but inertial oscillations are allowed, consistent with Tandon and Garrett (1994). When both the  $Fr = 0.1$  and  $Fr = 1.0$  cases begin to produce wavelike disturbances along the front as in Fig. 2 (Boccaletti et al., 2007; Fox-Kemper et al., 2008), we switch resolutions to those listed in Table 1 in order to compute the subsequent finite-amplitude growth phase of these instabilities.

Geostrophic scaling implies that the order of magnitude difference in  $Fr$  will produce an order of magnitude smaller velocity field in the weakly-stratified case compared to the strongly-stratified case. In order to compare the evolution of both systems on

dynamically consistent times, we nondimensionalize time throughout with the eddy turn over time scale estimated from the horizontal enstrophy

$$\tau^* = \left( \overline{\left( \frac{\partial v}{\partial x} - \frac{\partial u}{\partial y} \right)^2} \right)^{-\frac{1}{2}}, \quad (5)$$

where the overline denotes spatial averaging. These time scales are computed for each flow over a strip of  $3 \text{ km} \leq y \leq 6 \text{ km}$  for all  $x$  along horizontal surfaces at 5 m depth coinciding with the area of frontal instability. The  $\tau^*$  values differ by exactly an order of magnitude, namely  $\tau^*(Fr = 1.0) / \tau^*(Fr = 0.1) = 10$ , quantifying the slow evolution of the mixed layer instability in the case of the weakly-stratified front.

The snapshot of the 3D density perturbation  $\rho'$  for  $Fr = 0.1$  at  $t/\tau^* = 64$  (15 days) is shown in Fig. 2b, which displays clear coherent vortices with scales consistent with  $\mathcal{R} \approx 2$  km, and visually similar to those simulated by Boccaletti et al. (2007), Fox-Kemper et al. (2008), Thomas et al. (2008), Mahadevan et al. (2010). The eddies near the surface are generally anticyclonic, while the eddies propagating in the opposite direction along the base of the mixed layer tend to be cyclonic (Fig. 3). The exchange flow during the restratification, combined with strong stratification create a highly surface-intensified and vertically-sheared velocity field (Fig. 4a), even though the visualization of the surface flow field through the  $\rho'$  field gives, somewhat misleadingly, the impression of 2D geostrophic turbulence. The part of the domain below the mixed layer is likely to be rich with internal wave activity, but this issue is not investigated here. The exchange flow associated with restratification reaches the limits of our domain at about at  $t/\tau^* = 128$  (30 days) (Fig. 2c), shortly after which we terminate the integration since boundary induced shears and flows become important beyond that stage.

The simulation with  $Fr = 1.0$  is characterized by much smaller eddies, the scale of which is consistent with  $\mathcal{R} \approx 0.2$  km (Fig. 2d,e). These features persist not only across the entire mixed layer but their velocity signature appears to penetrate across the entire depth of the domain (Fig. 4b). In this regime of weak stratification, rotational dynamics appear to dominate and impose Taylor columns. As such, despite looking like 3D breakdown from their surface signature, this regime has a strong barotropic component and relatively weak vertical shear.

To quantify the dynamic regimes of the evolving flow fields, we compute the time dependence of volume averaged potential and kinetic energy quantities. Changes in the stratification of the system produced by the mixed layer instabilities are accurately estimated by tracking changes in the background (or reference) potential energy, RPE (Winters et al., 1995). RPE is the minimum potential energy that can be obtained through an adiabatic redistribution of the water masses, and it is computed using the probability density function approach introduced by Tseng and Ferziger (2001). In this method, the fluid is scanned every time step and the fluid parcels with a density perturbation  $\rho'$  within the range of  $[0, \Delta \rho']$  are assigned into bins between  $\rho$  and  $\rho + d\rho$ . The normalized number of control volumes in each bin gives the probability density function  $P(\rho) = V^{-1} \int_V \delta(\rho - \rho') dV$ , where  $\delta(\cdot)$  is the Dirac delta function.  $P(\rho)$  is the probability that a given fluid parcel has density  $\rho$ . Next, we define  $z_r(\rho')$  to be the height of fluid of density  $\rho'$  in the minimum potential energy state, which can be computed as  $z_r(\rho') = H \int_{\rho'}^{\Delta \rho'} P(\rho) d\rho$ . The background potential energy is calculated from

$$RPE = gL^2 \int_0^H \bar{\rho}'(z_r) z_r dz_r, \quad (6)$$

by splitting the computed  $\bar{\rho}'$  distributions into 51 bins at each time step.

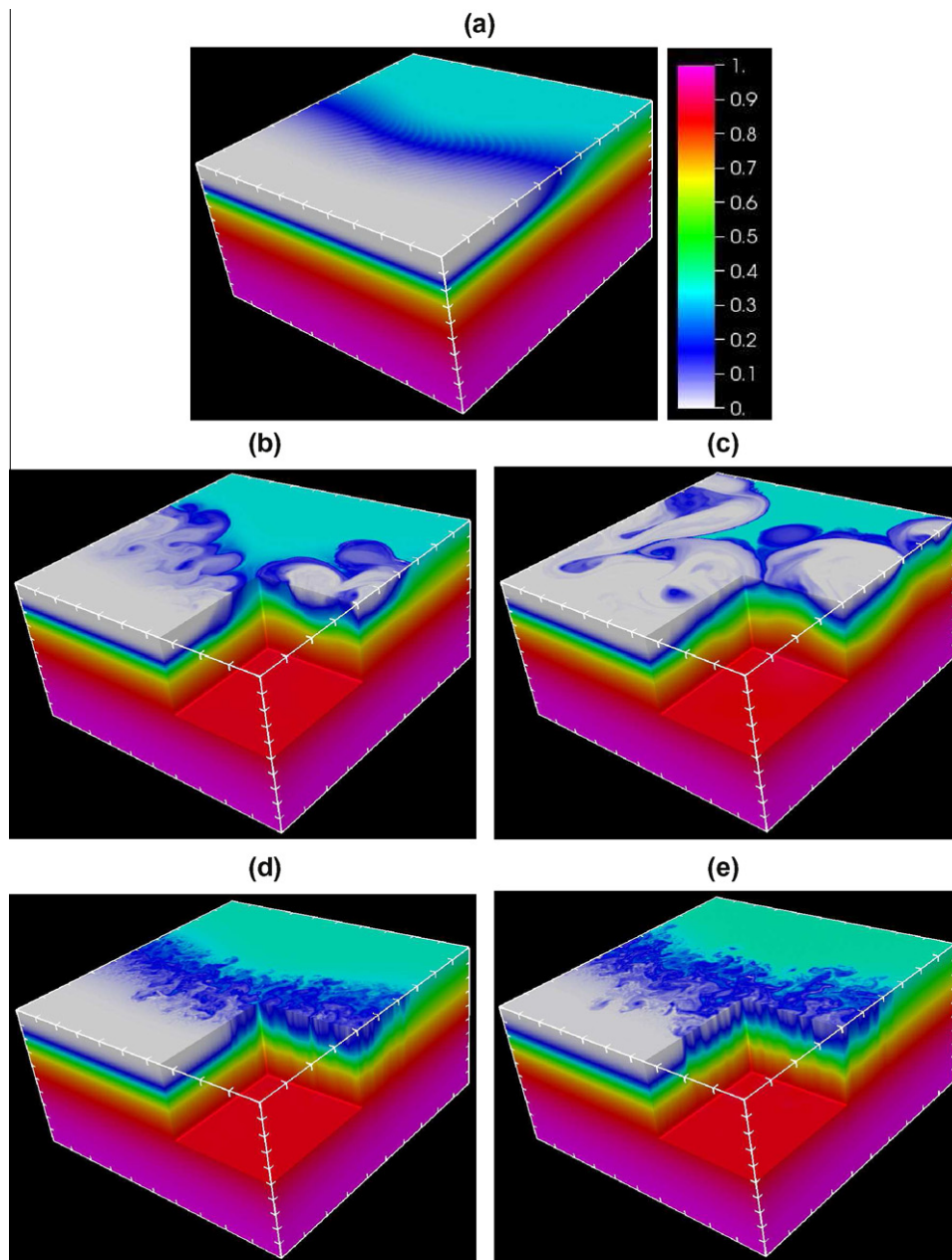


**Fig. 2.** Density perturbation field  $\bar{p}$  (a) at the onset of fine-scale instabilities, the state of the strongly-stratified case  $Fr = 0.1$  at (b)  $t/\tau^* = 64$ , (c)  $t/\tau^* = 128$ , and the state of the weakly-stratified case  $Fr = 1.0$  at (d)  $t/\tau^* = 74$ , and (e)  $t/\tau^* = 120$ . The thick marks are placed every 1 km in the horizontal and 50 m in the vertical directions.

Fig. 5a shows the deviation of the background potential energy from its initial state ( $RPE(t) - RPE(0)$ ) in both the strongly and weakly stratified flows. Mixed-layer instabilities in the  $Fr = 0.1$  flow produce an initial period of non-mixing internal oscillations before a transition to fully non-linear evolution approximately 10–12 days after initialization ( $t/\tau^* \sim 50$ ). Absolute mixing is much smaller in the less energetic weakly stratified flow.

To compare the relative mixing in the two flows, the evolution of the  $Fr$ -independent, relative background potential energy,

$$RPE^*(t) \equiv \frac{RPE(t) - RPE(0)}{RPE(0)}, \quad (7)$$

is shown in Fig. 5b. The rescaling shows that the  $Fr = 1.0$  flow exhibits a similar initial phase ( $t/\tau^* < 5$ ) during which little or no irreversible mixing takes place. The time scale for the transition to energetic mixing is again  $\sim 10$ –12 days. While the smaller-scale structures in

the  $Fr = 1.0$  flow produce more relative mixing, the disparity of time scales implies that the rate of relative mixing is nearly identical in both the strongly and weakly stratified situations.

Fig. 6 shows comparisons of the time evolution of the zonal mean and eddy kinetic energy in the two flows. Here the mean is defined by averaging in the periodic, along-front direction. The time-dependent mean (MKE) and eddy kinetic (EKE) energies are computed by volume averaging over  $x$ - $y$  planes in the top 100 meters of the water column. For both stratifications, non-linear evolution of mixed-layer instabilities produce eddy dominated flows after approximately 20 days. In what follows, we concentrate attention on flows during those time periods ( $t/\tau^* \geq 60$ ) where the mixed layer instabilities have reached a fully non-linear mixing state characterized by rapid growth in the reference potential energy and  $EKE > MKE$ .

Although appropriately re-scaled measures of volume averaged kinetic and potential energy behave similarly for both the  $Fr = 0.1$

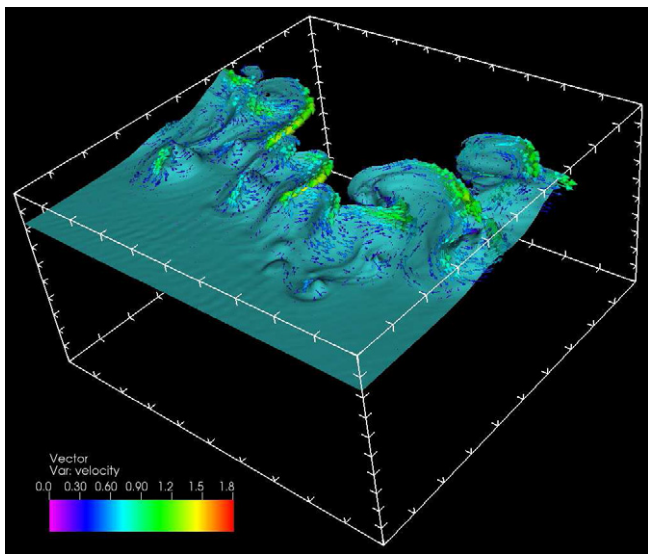


**Fig. 3.** Velocity vectors along the  $\bar{\sigma} = 0.2$  isopycnal for strongly-stratified  $Fr = 0.1$  case at  $t/\tau^* = 64$ . The color bar shows non-dimensional velocity magnitude (1 non-dimensional unit corresponds to 0.02 m/s), and thick marks are placed every 1 km in the horizontal and 50 m in the vertical directions. (For interpretation of the references to color in this figure legend, the reader is referred to the web version of this article.)

and  $Fr = 1.0$  flows, changes in stratification have marked effect on the spectral energy distribution once instabilities reach the fully non-linear regime. Wavenumber spectra of the normalized kinetic energy for the two flows are shown in Fig. 7. The spectra were computed by averaging over 56 one-dimensional spectra taken along the periodic direction at cross-stream locations stated above. For  $Fr = 0.1$ , the spectra show approximately one decade of forward enstrophy cascade,  $k^{-3}$ , scaling. The less stratified  $Fr = 1.0$  flow shows indications of both forward enstrophy and  $k^{-5/3}$  inverse energy cascade ranges. These differences are consistent with the differences in the initial forcing scale,  $\mathcal{R}$ , as described in Section 3. Given the finite size of the computational domain, the strongly stratified flow is forced at scales only slightly smaller than the domain size ( $\frac{\mathcal{R}}{L} \approx 0.2$ ) thus prohibiting the development of an inverse energy cascade.

### 5. Sampling strategies

We now focus on the feasibility of synoptic sampling of the flow fields produced once the mixed layer instabilities have reached a fully non-linear state. We consider the use of large arrays of Lagrangian drifter measurements and releases of passive scalar patches.

#### 5.1. Sampling with Lagrangian particles

##### 5.1.1. Relative dispersion

Several diagnostics can be considered using clusters of Lagrangian particles advected by the flow field. One of the commonly used metrics is the absolute (or single-particle) dispersion,

$$A^2(t, t_0) = \frac{1}{M} \sum_{i=1}^M |\mathbf{x}_i(t) - \mathbf{x}_i(t_0)|^2 = \langle |\mathbf{x}_i(t) - \mathbf{x}_i(t_0)|^2 \rangle, \quad (8)$$

which quantifies the average distance covered in time by  $M$  Lagrangian particles following their release at  $t = t_0$ , and it is useful to characterize the mean circulation, or the fate of particles (Falco et al., 2000; Fratantoni, 2001).

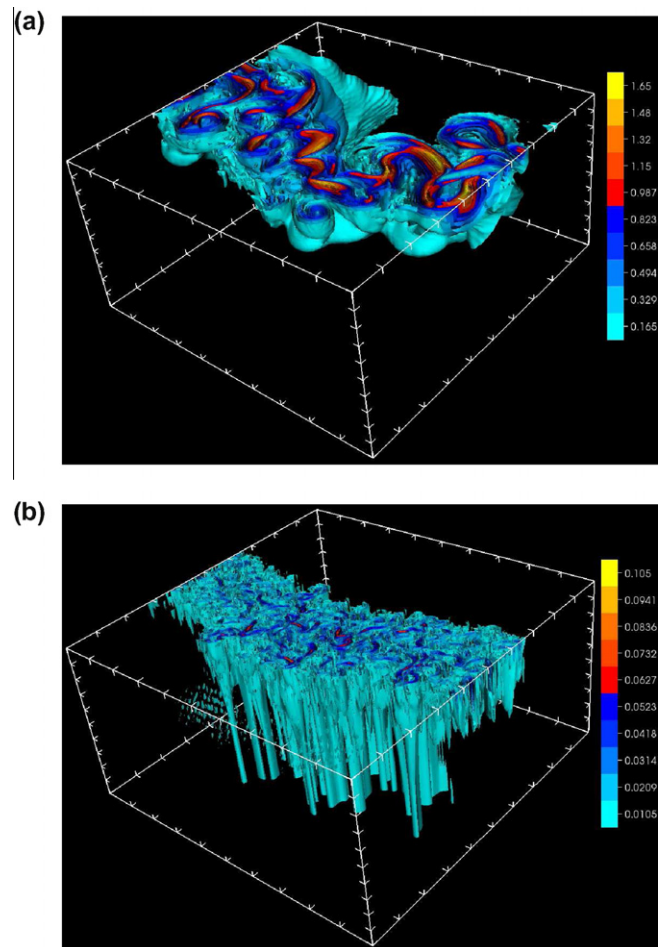


**Fig. 4.** Three-dimensional contours of velocity magnitude (1 non-dimensional unit corresponds to 0.02 m/s) for (a) the strongly-stratified case  $Fr = 0.1$  at  $t/\tau^* = 64$ , and (b) the weakly-stratified case  $Fr = 1.0$  at  $t/\tau^* = 74$ . The color bars show non-dimensional velocity magnitudes, and thick marks are placed every 1 km in the horizontal and 50 m in the vertical directions. (For interpretation of the references to color in this figure legend, the reader is referred to the web version of this article.)

Another Lagrangian metric that is more closely tied to mixing processes is the relative (two-particle) dispersion,

$$D^2(t) = \langle |\mathbf{x}^{(1)}(t) - \mathbf{x}^{(2)}(t)|^2 \rangle, \quad (9)$$

where the average is over all pairs of particles in the cluster. Thus, relative dispersion quantifies the mean-square particle separation. The reader is referred to Bennett (1984), Sawford (2001), LaCasce (2008), Poje et al. (2010) and Haza et al. (2010) for reviews and recent estimations of relative dispersion for oceanic flows.

Relative dispersion defined in (9) tends to give oscillatory behavior especially when a small number of particles are used (Lacorata et al., 2001). The root cause is that the average in (9) is taken over a wide range of separation scales at any one time and tends to be dominated by those particle pairs with the largest separations. To address this issue, a complementary measure, namely the Finite-Scale Lyapunov Exponent (FSLE, Aurell et al., 1997; Artale et al., 1997) is often employed:

$$\lambda(\delta) = \frac{\ln(\alpha)}{\langle \tau(\delta) \rangle}, \quad (10)$$

where  $\langle \tau(\delta) \rangle$  is the averaged time (over the number of particle-pairs) required to separate from a distance of  $\delta$  to  $\alpha\delta$ . The FSLE provides a measure of relative dispersion as a function of separation

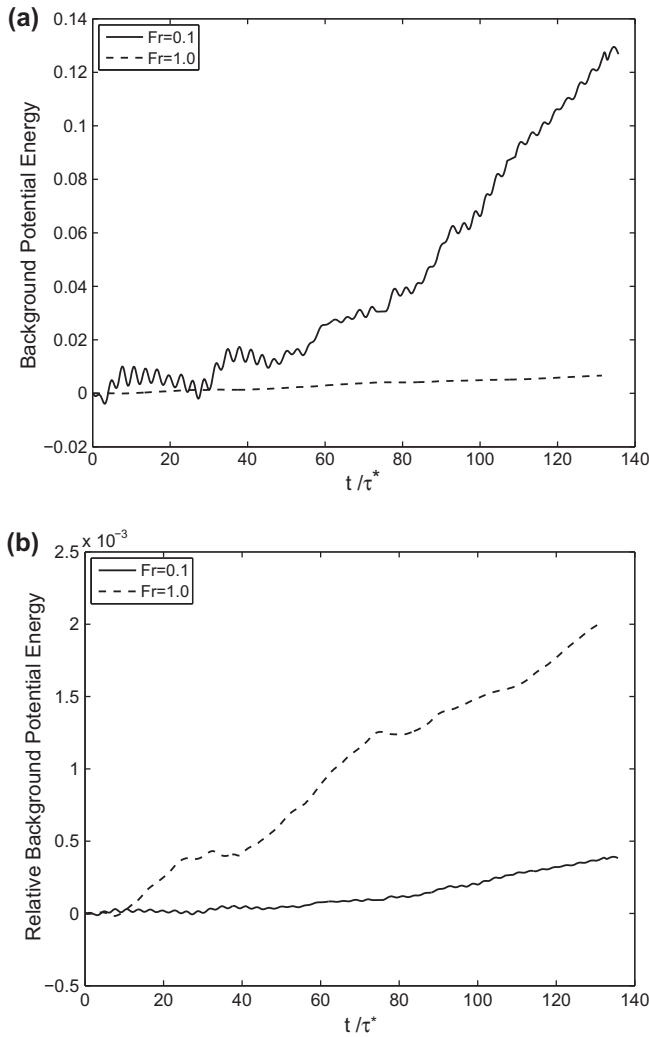


**Fig. 5.** Evolution of (a) background potential energy from its initial state and (b) relative background potential energy  $RPE^*$  with scaled time  $t/\tau^*$  in flows with  $Fr = 0.1$  (solid) and  $Fr = 1.0$  (dashed).

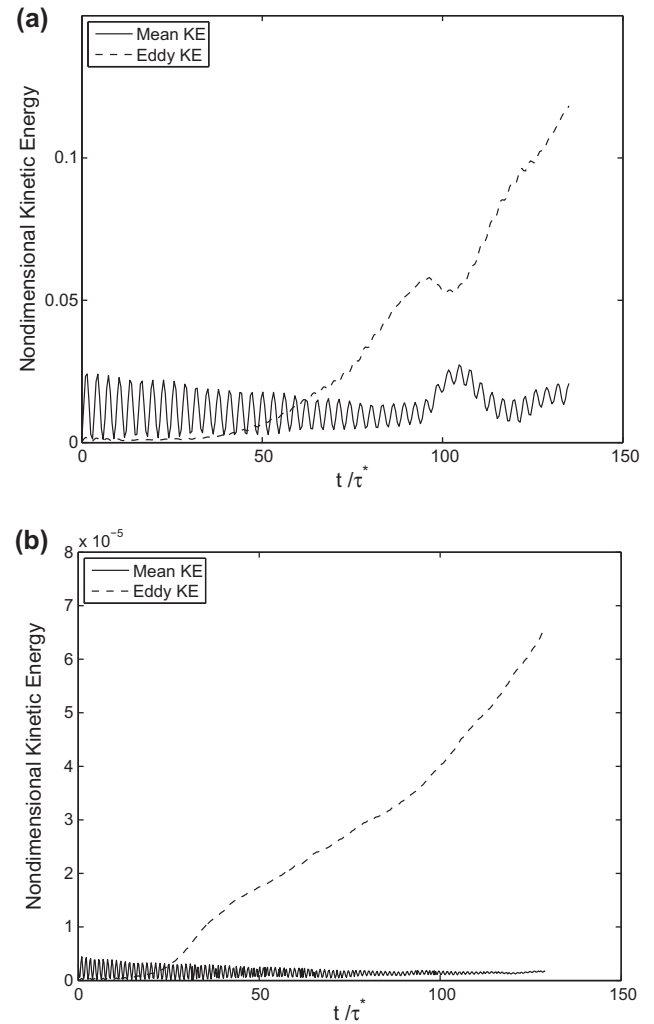


**Fig. 6.** Time evolutions of mean (solid) and eddy (dashed) kinetic energies for the upper 100 m in the domain in (a) strongly-stratified ( $Fr = 0.1$ ) and (b) weakly-stratified ( $Fr = 1.0$ ) cases.

scale and serves to isolate different dispersion regimes at those scales (Haza et al., 2008).

### 5.1.2. Sampling strategy

The scale-dependent FSLE  $\lambda(\delta)$  is computed as follows. Particles are released over a  $1 \text{ km} \times 1 \text{ km}$  area coinciding with intense mixed layer instabilities ( $2.5 \text{ km} \leq x \leq 3.5 \text{ km}$  and  $4 \text{ km} \leq y \leq 5 \text{ km}$ ). The initial location is chosen close to the left of the domain in order to account for advection along the front (Fig. 8). Within this region,  $25 \times 25$  triplets are released (1875 particles) where the two satellite particles are 19.5 m apart from the center particles. This configuration is repeated at depths levels of  $z_0 = 5 \text{ m}$  (near surface),  $z_0 = 50 \text{ m}$  (middle of the mixed layer) and  $z_0 = 100 \text{ m}$  (mixed layer base).

While advecting a total of 5625 particles online, two different schemes are used. In the first one, fully 3D velocity fields are used ( $\frac{dx}{dt} = u$ ,  $\frac{dy}{dt} = v$ ,  $\frac{dz}{dt} = w$ ), which gives rise to Lagrangian trajectories depicted in Fig. 9a,b for the strongly-stratified ( $Fr = 0.1$ ) and weakly-stratified ( $Fr = 1.0$ ) cases, respectively. Nevertheless, while readily feasible in the context of LES, fully 3D Lagrangian floats (D'Asaro et al., 1996) are not yet economical enough to deploy in large numbers. As such, synthetic particles are advected also in a

2D sense ( $\frac{dx}{dt} = u$ ,  $\frac{dy}{dt} = v$ ,  $z = z_0$ ) in order to explore the differences from 3D advection (Fig. 9c and d).

The FSLE  $\lambda(\delta)$  is computed using  $\alpha = \sqrt{2}$  in (10), which is a common value (Aurell et al., 1997; Lacorata et al., 2001; LaCasce and Ohlmann, 2003). We use original pairs initially and rely on chance pairs (namely those particles that approach one another at some time after the initial launch) at larger  $\delta$  in order to maintain high pair numbers;  $\lambda(\delta)$  is plotted only as long as the pair number is larger than 100 to ensure the accuracy of results.

The scale-dependent FSLE  $\lambda(\delta)$  from particle launches at 5 m horizontal planes are depicted in Fig. 10a. The strongly-stratified case ( $Fr = 0.1$ ) exhibits a clear exponential regime from separation scales of 20 m to about 1 km, whereas in the weakly-stratified case ( $Fr = 1.0$ ), the extent of the exponential regime is much smaller, confined approximately to a range of  $20 \text{ m} \leq \delta \leq 100 \text{ m}$ . In order show the trends better, we have conducted an additional experiment with an intermediate stratification,  $Fr = 0.31$ , which falls in the middle of the other two. This plot is consistent with the ideas put forth in Poje et al. (2010) in that the extent of the exponential regime is related to the spatial scale range of the smooth velocity fields, which differ by approximately by an order of magnitude between the two cases with  $Fr = 0.1$  and  $Fr = 1.0$ . This FSLE plot also indicates that the scale of the coherent vortices is well estimated

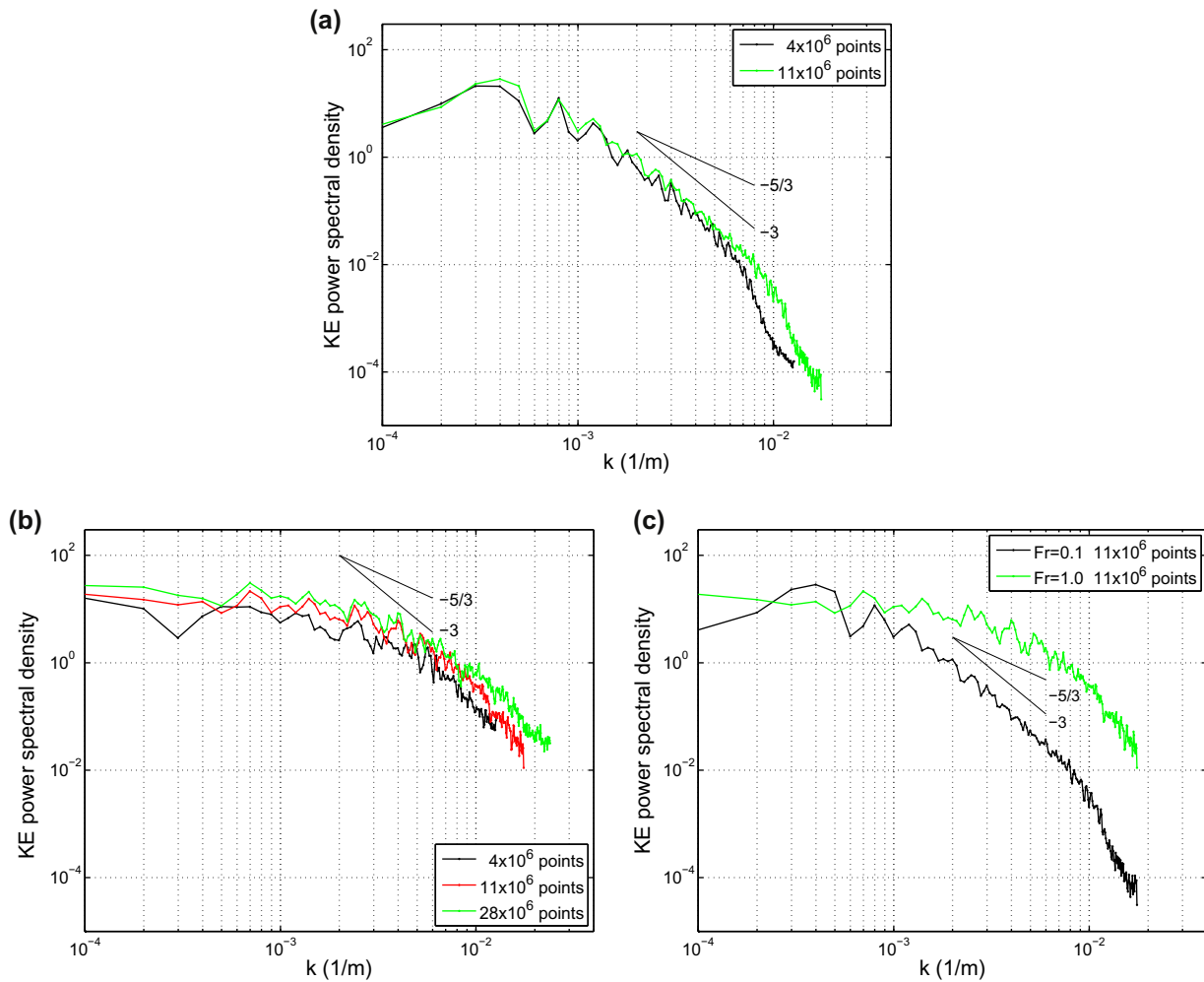


**Fig. 7.** Normalized kinetic energy power wavenumber spectra of (a) strongly-stratified ( $Fr = 0.1$ ) case with standard and high-res1 resolutions at  $t/\tau^* = 64$ ; (b) weakly-stratified ( $Fr = 1.0$ ) case with standard, high-res1 and high-res2 resolutions at  $t/\tau^* = 74$ ; (c) superposition of spectra from  $Fr = 0.1$  and  $Fr = 1.0$  with high-res1 resolution.

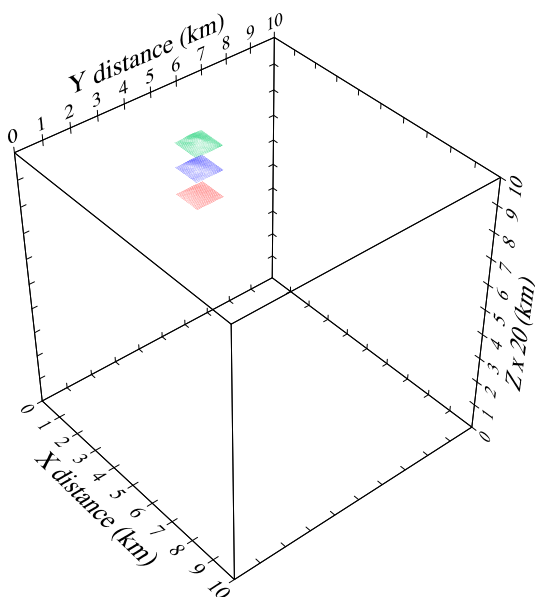


**Fig. 8.** Initial drifter release in a  $1\text{ km} \times 1\text{ km}$  patch formed by  $25 \times 25 = 625$  triplets (1875 particles) at depth levels of 5 m (green), 50 m (blue) and 100 m (red). (For interpretation of the references to color in this figure legend, the reader is referred to the web version of this article.)

by  $\mathcal{R}$ . Physically, this indicates that the hyperbolicity induced by the mixed layer eddies dictates relative dispersion, i.e., it is non-local (Bennett, 1984) at separation scales smaller than the size of the coherent eddies. It is certainly desirable to investigate how these curves would be modified in a more realistic setting involving more processes than mixed layer instability, namely in the presence of mesoscale straining field, or a truly resolved multi-scale setting including high-frequency surface forcing.

The range of limiting FSLE seen in Fig. 10a, approximately from  $0.2\text{ days}^{-1}$  to  $2\text{ days}^{-1}$ , falls within the range of existing oceanic observations. LaCasce and Ohlmann (2003) obtained  $\lambda_{max} \approx 0.3\text{ days}^{-1}$  from SCULP drifters in the Gulf of Mexico, Schroeder et al. (2011) estimated  $0.7 \leq \lambda_{max} \leq 1.5\text{ days}^{-1}$  from CODE drifters in the Ligurian Sea, Koszalka et al. (2009) found  $\lambda_{max} \approx 0.5\text{ days}^{-1}$  from POLEWARD drifters in Nordic Seas. There are two other estimates that gave significantly higher values than these. The first is by Haza et al. (2010), who computed  $4 \leq \lambda_{max} \leq 7\text{ days}^{-1}$  on the basis of VHF-radar derived velocity fields in the Gulf of La Spezia. This is likely to be due to the complex geometry of this gulf. Lumpkin and Elipot (2010) estimated  $\lambda_{max} \approx 10\text{ days}^{-1}$  from SVP drifters in the Gulf Stream region under strong wind and wave action in the winter. This last value is very interesting since it is likely to reflect relative dispersion under the action of intense submesoscale features in the upper ocean. For separation scales larger than the scale of the energy-containing, coherent eddies, we find a scaling

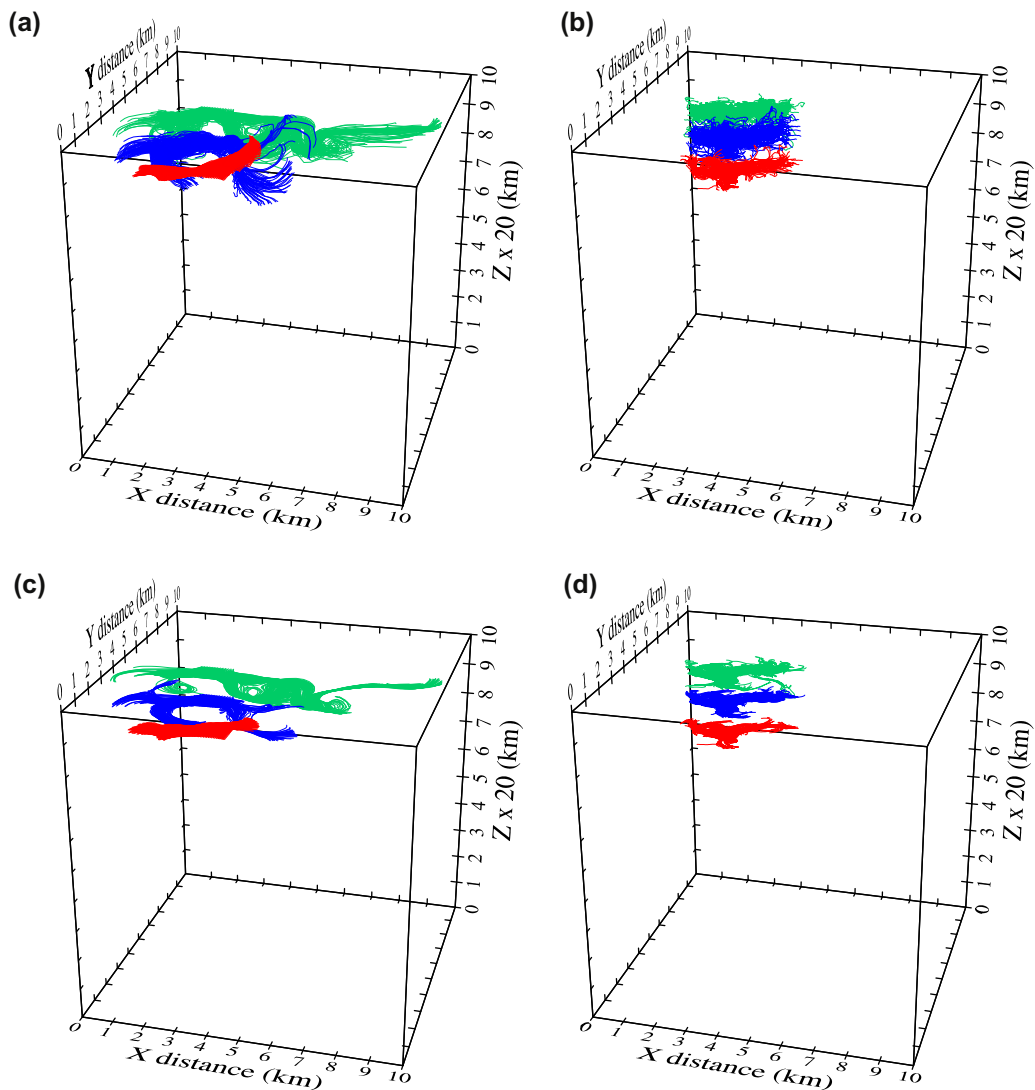


**Fig. 9.** Lagrangian trajectories in the strongly-stratified  $Fr = 0.1$  (a) and weakly-stratified  $Fr = 1.0$  (b) cases with 3D particle advection. Same using 2D advection is shown in (c) and (d). Vertical axis is stretched 20-fold.

consistent with the Richardson regime,  $\lambda \sim \delta^{-2/3}$ , which is quite general, as discussed in Poje et al. (2010), and references therein.

Results by Poje et al. (2010) and Haza et al. (2010) from ocean circulation models indicate that the maximum value of the  $\lambda$  scales with the resolution of Eulerian velocity gradients as given by the average of positive Okubo–Weiss parameter values. In particular, a good correlation was found with positive (hyperbolic) values of the Okubo–Weiss partition

$$Q^+ = A^{-1} \int \sqrt{Q} dA, \quad \text{for } Q > 0, \quad (11)$$

where  $Q = S^2 - \omega^2 = \left(\frac{\partial u}{\partial x} + \frac{\partial v}{\partial y}\right)^2 + 4\left(\frac{\partial u}{\partial y} \frac{\partial v}{\partial x} - \frac{\partial u}{\partial x} \frac{\partial v}{\partial y}\right)$  is the Okubo–Weiss criterion (Okubo, 1970; Weiss, 1991),  $S^2 = \left(\frac{\partial u}{\partial x} - \frac{\partial v}{\partial y}\right)^2 + \left(\frac{\partial v}{\partial x} + \frac{\partial u}{\partial y}\right)^2$  is the square of the horizontal strain rate,  $\omega^2 = \left(\frac{\partial v}{\partial x} - \frac{\partial u}{\partial y}\right)^2$  the square of horizontal vorticity, and  $A$  is the area of the mixed layer instability. Therefore, it is reasonable to expect that mixed layer flows driven by high lateral stratifications (high  $Fr$ ) will lead to high strain rate, and to higher  $\lambda$  at the smallest separation

scales. The rescaled FSLE,  $\lambda/Q^+$ , shows an excellent collapse over the exponential ranges of the FSLEs (Fig. 10b).

### 5.1.3. Depth-dependence of the FSLE

It is of interest to study how relative dispersion varies with depth. Fig. 11a indicates that in the strongly-stratified case ( $Fr = 0.1$ ), the maximum value of the FSLE reduces from  $\lambda_{max} \approx 2 \text{ days}^{-1}$  for 5-m releases to  $\lambda_{max} \approx 1 \text{ days}^{-1}$  for 50-m releases, and to less than  $\lambda_{max} \approx 0.5 \text{ days}^{-1}$  at 100 m, indicating longer particle separation times with depth. A similar reduction (by approximately a factor of 2 at the selected depth levels) in  $\lambda_{max}$  is also seen for the weakly-stratified case (Fig. 11b).

While  $\lambda_{max}$  is depth dependent, it is not quite clear what role vertical velocities play in particle separation with respect to reduced horizontal hyperbolicity with depth. Note that the initial particle launch at constant depth (Fig. 8) serves to separate these two factors. We keep in mind the high aspect ratio ( $L/h_0 = 125$ , where  $h_0 \approx 80 \text{ m}$ ) of the mixed layer, that implies two orders of magnitude difference between horizontal and vertical velocities by scaling of the continuity equation. This is quantified by using the ratio of  $U_{rms} = \sqrt{u^2 + v^2}$  and  $W_{rms} = \sqrt{w^2}$  where the spatial

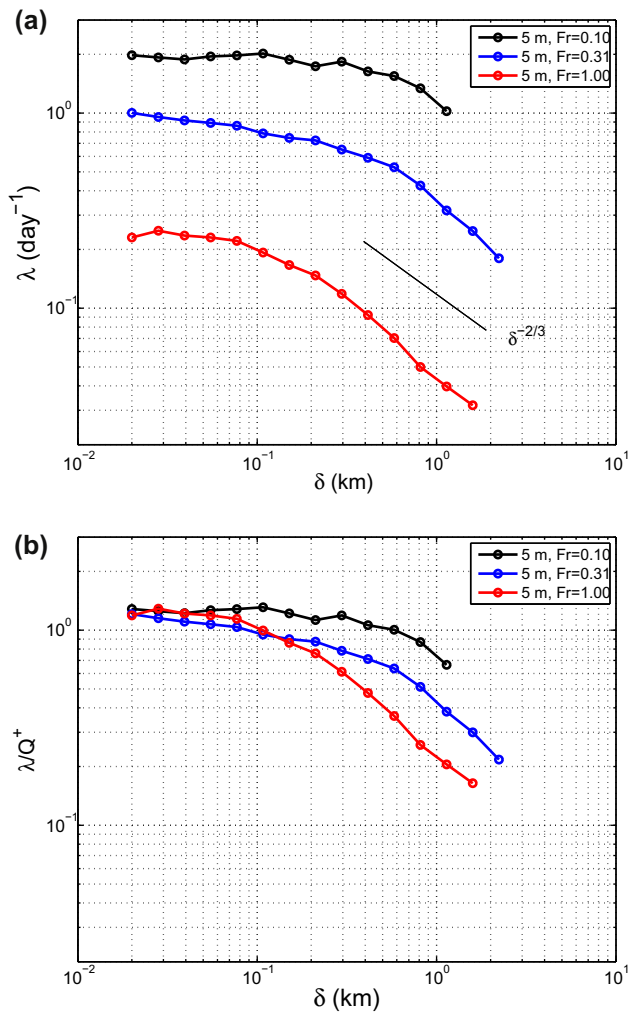


**Fig. 10.** (a) Dependency of the FSLE  $\lambda(\delta)$  on the  $Fr$  from 5 m particle releases; strongly-stratified flow ( $Fr = 0.1$ , black), weakly-stratified flow ( $Fr = 0.1$ , red) and an intermediate case ( $Fr = 0.31$ , blue) are plotted. The slopes in the background indicate relative dispersion corresponding to the Richardson ( $\delta^{-2/3}$ ) regime. (b) Same as (a) after rescaling  $\lambda$  with  $Q^*$  in each flow. (For interpretation of the references to color in this figure legend, the reader is referred to the web version of this article.)

averaging is taken  $3 \text{ km} \leq y \leq 6 \text{ km}$  for all  $x$  at different depths. Table 2 clearly indicates that  $U_{rms}/W_{rms}$  is large enough for vertical displacements not to play a major role in particle separation. The collapse of the  $\lambda_{max}$  using  $Q$  implies that horizontal processes dominate the initial particle separation. One can thus expect that the role of vertical velocities are even smaller for larger separation distances. In order to provide quantitative insight into this question, the FSLE curves from 3D and 2D particle advection are compared in Fig. 11. The results show no significant difference, indicating that when particles are released at horizontal surfaces, their relative dispersion is dominated by horizontal processes. In other words, the vertical separations are much smaller with respect to horizontal separations, as indicated also visually in Fig. 9. This result is likely to be modified if the mixed layer experiences active wind and wave driven mixing with significant vertical transport.

#### 5.1.4. Turbulent coherent structures

The spatial maps of the FSLE (and related metric the finite-time Lyapunov exponent FTLE, Haller (1997)) are employed increasingly more often in the Lagrangian analysis of oceanic flow fields (d'Ovidio et al., 2004; Olascoaga et al., 2006; Haza et al., 2007,

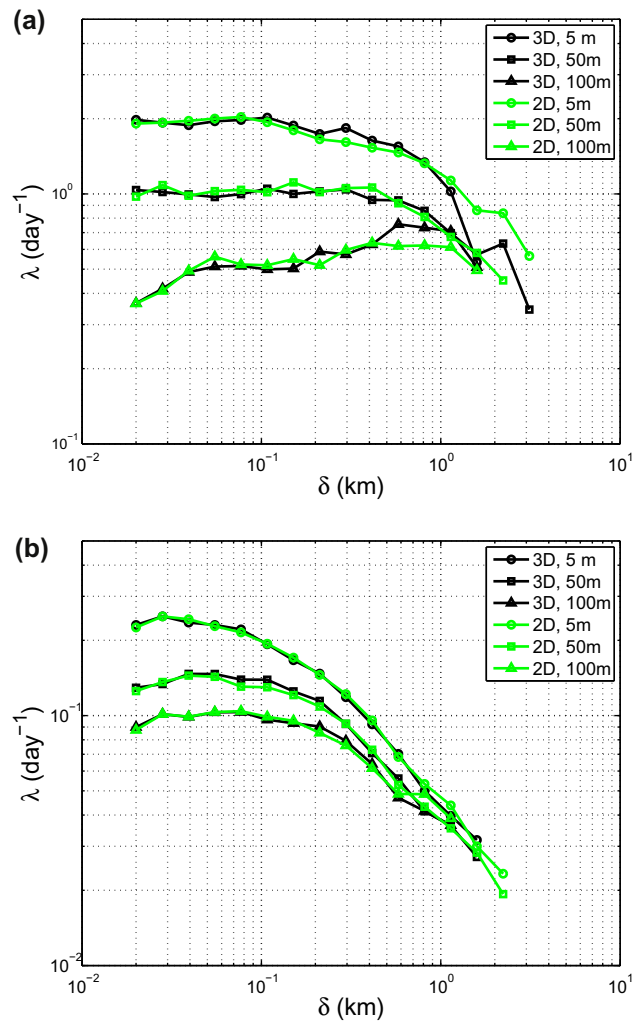


**Fig. 11.** The FSLE  $\lambda(\delta)$  from releases at three depth levels as well as 3D (black) and 2D (green) particle advection for the (a) strongly-stratified ( $Fr = 0.1$ ), and (b) weakly-stratified ( $Fr = 1.0$ ) cases. (For interpretation of the references to color in this figure legend, the reader is referred to the web version of this article.)

**Table 2**

The ratio of  $U_{rms} = \sqrt{u^2 + v^2}$  and  $W_{rms} = \sqrt{w^2}$  spatially averaged over a range of  $3 \text{ km} \leq y \leq 6 \text{ km}$  for all  $x$  at different depths at beginning of the drifter sampling in strongly and weakly-stratified flow fields.

$U_{rms}/W_{rms}$	5 m	50 m	100 m
$Fr = 0.1$	175	51	41
$Fr = 1.0$	37	33	52

2008; Shadden et al., 2008; Poje et al., 2010; Haza et al., 2010). This is because spatial maps of the FSLE are found (e.g., Molcard et al., 2006) to be accurate and computationally-efficient proxies for the Lagrangian Coherent Structures (LCS). LCS are material surfaces controlling transport, that have been traditionally estimated on more complex algorithms centered around the identification of finite-time hyperbolic trajectories (Ottino, 1989; Haller and Poje, 1998; Poje and Haller, 1999; Couliette and Wiggins, 2000; Miller et al., 2002; Wiggins, 2005).

Next, we employ spatial maps of the FSLE in order to visualize turbulent coherent structures responsible for transport in the mixed layer instability problem. This is done on the basis of releasing and advecting 390,963 particles at 5 m depth in the flow fields (Fig. 12a, Fig. 13a). It is done in 2D because the dynamical system

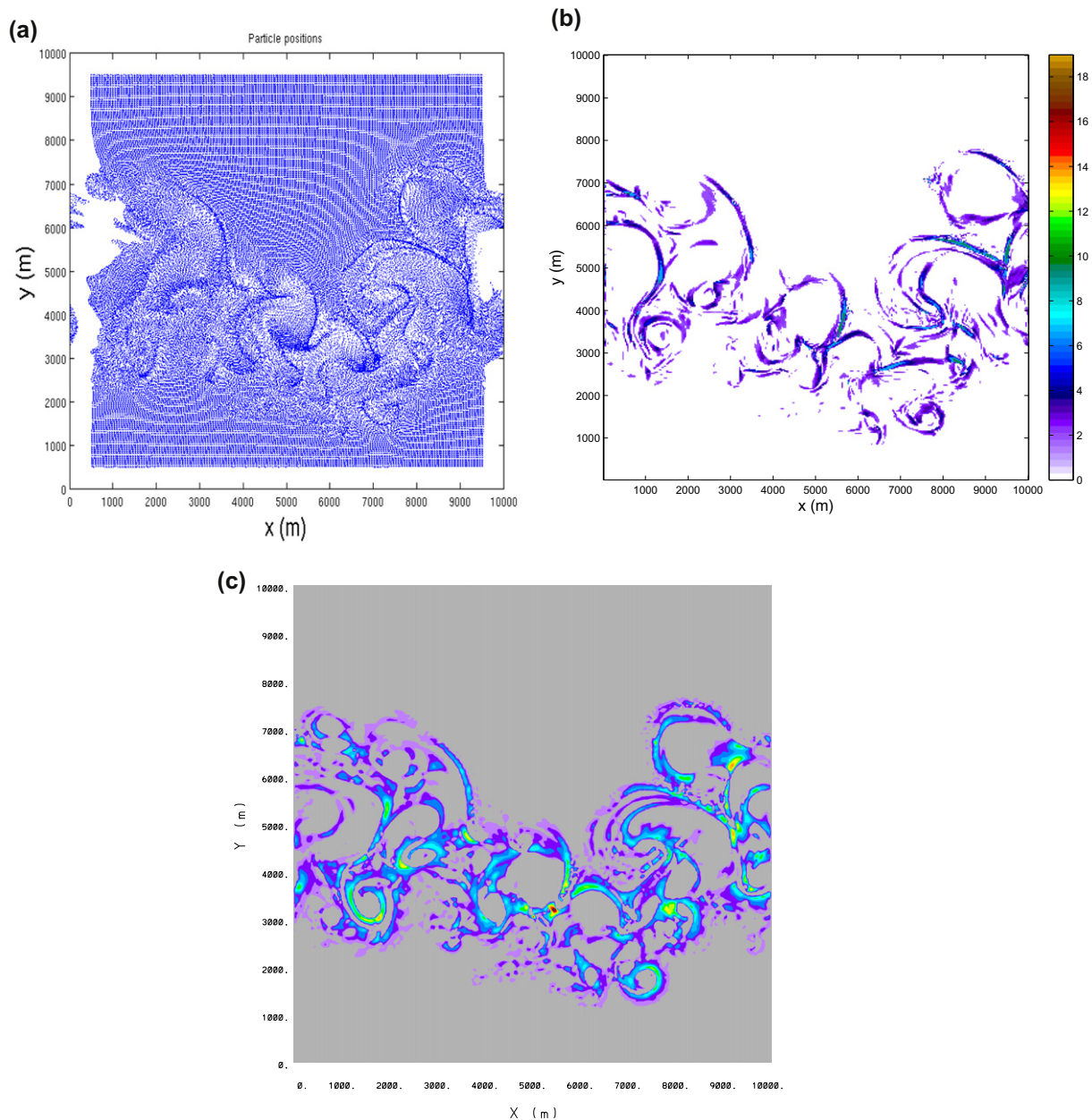


**Fig. 12.** (a) Particle positions after about half a day of advection, (b) the FSLE map (color scale is in days<sup>-1</sup>), and (c) positive eigenvalues (normalized by the maximum) of the velocity gradient tensor at 5 m depth for the strongly-stratified case ( $Fr = 0.1$ ). (For interpretation of the references to color in this figure legend, the reader is referred to the web version of this article.)

theory for 3D is not yet well developed, and we do not want to extend proxies for LCS to 3D at this point. Forward time integration emphasizes regions of concentration, typically associated with stable manifolds, which are barriers to transport. In the strongly-stratified case ( $Fr = 0.1$ ), clear coherent structures are found (Fig. 12b), while the weakly-stratified case ( $Fr = 1.0$ ) yields features resembling isotropic turbulence (Fig. 13b).

Another approach is to identify regions of high hyperbolicity on the basis of the 2D tensor of velocity gradient  $\mathcal{A} \equiv \nabla \mathbf{u} = \begin{bmatrix} \frac{\partial u}{\partial x} & \frac{\partial u}{\partial y} \\ \frac{\partial v}{\partial x} & \frac{\partial v}{\partial y} \end{bmatrix}$ .

The hyperbolic regions are given by  $\gamma > 0$ , where  $\gamma$  are the eigenvalues found from  $\gamma^2 - \text{tr}(\mathcal{A})\gamma + \det(\mathcal{A}) = 0$  (Ottino, 1989). For non-divergent flow,  $\gamma = \sqrt{-\det(\mathcal{A})} = \left( \frac{\partial u}{\partial y} \frac{\partial v}{\partial x} - \frac{\partial u}{\partial x} \frac{\partial v}{\partial y} \right)^{1/2}$  for  $\det(\mathcal{A}) < 0$ . This criterion is equivalent to  $Q > 0$ . The difference between the FSLE and  $\gamma$  (or  $Q$ ) is that the latter is a Eulerian metric

that is applied to a frozen velocity field. Regions of  $\gamma > 0$  appear to highlight very similar features as with the FSLE maps (Figs. 12c and 13c), with the differences being due to effects of temporal variability over half a day of advection.

These results imply that the concept of LCS is most useful in flows when the lifespan of individual eddies is longer than the time it takes for fluid parcels to circulate in those eddies (as in Fig. 12b). On the other hand, if regions of strong hyperbolicity appear and disappear rapidly, transport barriers have a much more complex structure (Fig. 13b).

#### 5.1.5. Sensitivity to sampling area

In order to explore the uncertainty in the FSLE curves arising from spatial and temporal variations of the sampling, the size and location of the initial sampling patch shown in Fig. 8 are modified. Two other configurations are set up, in which the initial area

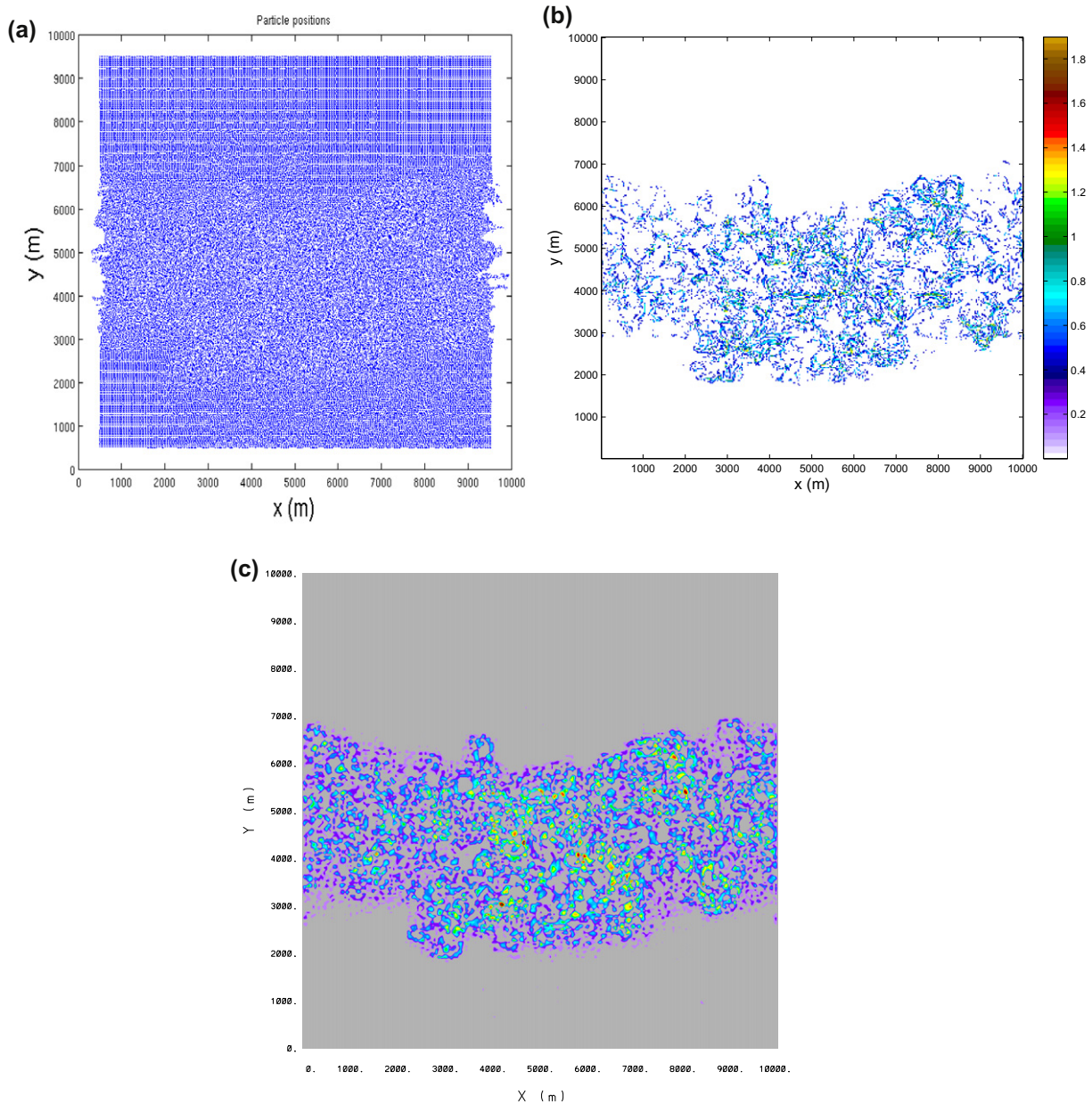


Fig. 13. Same as Fig. 12 but for the weakly-stratified case ( $Fr = 1.0$ ).

is enlarged to span  $2.5 \text{ km} \leq x \leq 4.5 \text{ km}$  and  $4 \text{ km} \leq y \leq 6 \text{ km}$ , and moved by 1 km in  $x$  and  $y$  directions. For the purpose of brevity, we do not include additional figures here, but report the results. We found that the FSLE curves do not show a major sensitivity to the size of the sampling area, but the limiting FSLE values can change by up to 35% when particles are released from another location within the mixed layer instability. This appears to be a reflection of the dependence of the limiting FSLE on the distribution of the hyperbolic regions coinciding with the initial launch area. Then, by keeping the original sampling area, the sampling time is shifted 24 eddy turnover time scales, and the results are found to be robust. These results are essentially consistent with the ideas put forward by Poje et al. (2002) and Molcard et al. (2006) in that launching drifters near regions of high hyperbolicity ensures good sampling coverage, and that  $\lambda_{max}$  is set by the horizontal strain rate in such regions (Poje et al., 2010).

#### 5.1.6. Sensitivity to the number of drifters

Possibly the most important question for sampling in an observational experiment is:

- How many drifters are needed in order to get reasonable estimates of  $\lambda(\delta)$ ?

This is because while thousands of drifters have been released in the ocean over the past few decades (e.g., Fratantoni (2001), <http://www.aoml.noaa.gov/phod/dac/dacdata.php>), the number of experiments in which clusters are deployed for the purpose to computing relative dispersion is quite limited (LaCasce and Ohlmann, 2003; Koszalka et al., 2009; Haza et al., 2010; Lumpkin and Elipot, 2010; Schroeder et al., 2011). In light of drifter cost, logistical problems of simultaneous deployment, tracking, and possible environmental concerns, the optimization of the

accuracy as a function of drifter numbers seems to be an important consideration.

In order to compute the variations in  $\lambda(\delta)$  as a function of number of drifters, the FSLE is computed by sub-sampled sets of particles consisting of 375, 96, and 27 particles, in comparison to the full set of 1875 particles. This is carried out for both  $Fr = 0.1$  and  $Fr = 1.0$ , and we focus on 5-m releases since these are the most energetic. The results (Fig. 14) show that even with 27 particles, the FSLE curves can be estimated fairly accurately. This is an encouraging result for observational programs, as it is not feasible to deploy thousands of drifters of present technology in the ocean without environmental implications.

Since the results shown in Fig. 14 correspond to single realizations, it is also of interest to compute statistics in order to identify any biases of such releases. Of particular interest is the case with 27 particles, since such a deployment is readily feasible at the present moment. For instance, 27 particles can be deployed easily in triplets as part of an experiment involving many other sampling platforms, while a much larger scale drifter deployment would almost certainly require a dedicated experiment with multiple ships. In order to obtain statistics, we have chosen 40 random sets of 27 particles in triplets. While choosing these particles, a trade off becomes apparent, which has an effect on a possible bias in results. One can either select particles to cover a small area initially, which would provide accuracy for  $\lambda_{max}$ , or distribute them over a larger area to ensure better estimates of  $\lambda$  at larger  $\delta$ . Here, we opted

for the first choice, given our interest in  $\lambda_{max}$ . We also imposed a minimum pair number of 10 in order to eliminate inclusion of estimates with high errors. Results shown in Fig. 15 indicate that the mean curves of  $\lambda$  from these ensembles of 27 particles have almost no bias, except for large  $\delta$  in the case with  $Fr = 1.0$ . This is perhaps due a combination of the limited integration period and initial sampling area discussed above. Releases targeted at circulation features and launch configurations to optimize multi-scale sampling are beyond the scope of this paper.

### 5.1.7. Sensitivity to model resolution

Despite the SGS model in the Boussinesq equations (1), the spatial filtering associated with LES also implies filtering of fast temporal scales (Sagaut, 2006), and the time-dependent turbulent motion of these unresolved scales can be important for particle dispersion. If this is the case, it implies effectively that SGS models should be incorporated not only in (1), but also in (3). Such Lagrangian SGS models have an established record in the context of single-particle dispersion (Griffa, 1996; Berloff and McWilliams, 2002; Veneziani et al., 2005; Haza et al., 2007), but have not been explored (to our knowledge) for relative dispersion problems.

In order to quantify the influence of the unresolved scales of motion on relative dispersion, the model resolution is increased by changing the polynomial order  $\mathcal{N}$  (Table 1). No significant

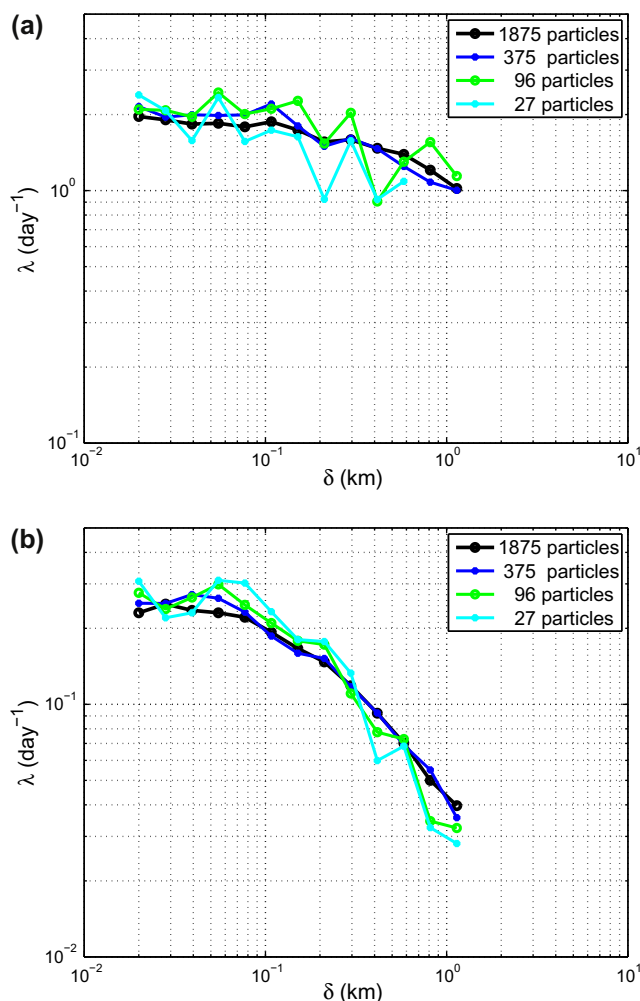


Fig. 14. Sensitivity of  $\lambda(\delta)$  to the number of particles in (a) strongly-stratified ( $Fr = 0.1$ ) and (b) weakly-stratified ( $Fr = 1.0$ ) cases from 5 m launches.

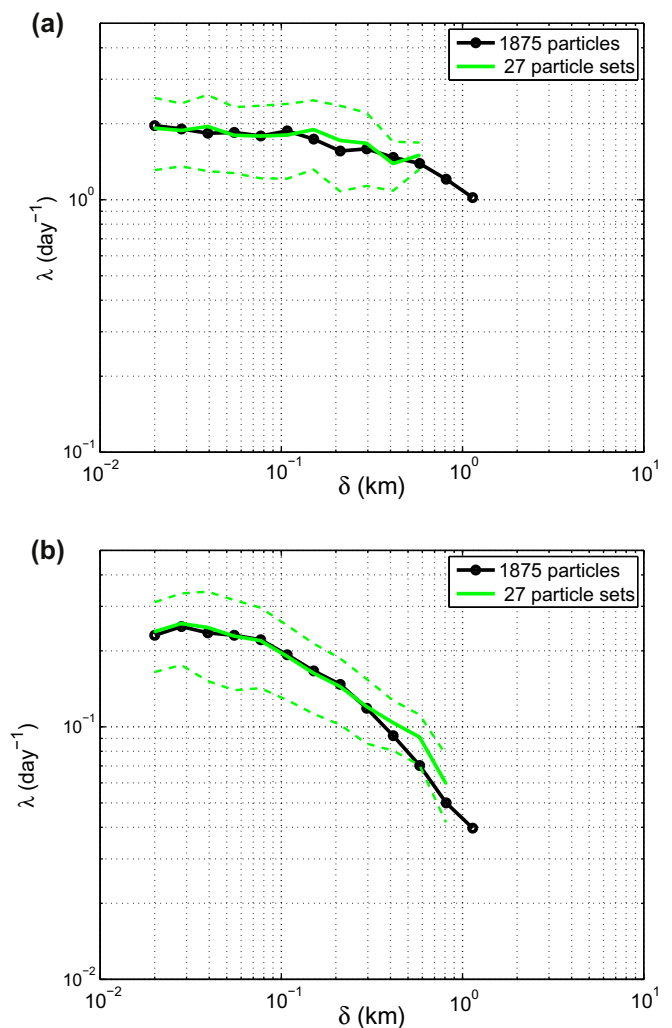


Fig. 15. The mean (solid) and standard deviation (dashed) of the  $\lambda(\delta)$  curves computed from ensembles each consisting of 27 particles in (a) strongly-stratified ( $Fr = 0.1$ ) and (b) weakly-stratified ( $Fr = 1.0$ ) cases from 5 m launches.

difference is seen between results from standard and high-res1 cases for flow fields with  $Fr = 0.1$  (not shown); as such, high-res2 is not computed. Obviously, the weakly-stratified case ( $Fr = 1.0$ ) is more challenging since it is characterized by eddies that are an order of magnitude smaller. Indeed, in this case we notice some impact on relative dispersion when finer scales of motion are resolved. The FSLE  $\lambda(\delta)$  changes for separation scales  $\delta \leq 100$  m (corresponding to eddy size of approximately  $2\Delta x$ , consistent with Nyquist sampling theorem) with decreasing mesh size. The limiting FSLE increases by approximately 22% from standard resolution to high-res1, and by 30% at high-res2. Given the converging behavior, we have not pursued more expensive computations. Clearly, there could be a need for Lagrangian SGS models in (3) in certain flow regimes, and the resolution-dependent  $\lambda(\delta)$  plots can provide a systematic framework for developing and testing such parameterizations in future studies.

### 5.2. Sampling with passive scalars

In addition to purely Lagrangian sampling using drifters, mixed layer processes can also be observed by tracking the evolution of controlled releases of a readily identifiable passive tracer (Ledwell et al., 1998; Sundermeyer and Ledwell, 2001). New observational techniques based on 3D mapping airborne lidar promise the ability to provide synoptic upper ocean concentration fields and mixing properties (Sundermeyer et al., 2007).

The evolution of a passive tracer is governed by the advection–diffusion equation given by Eq. (2). In the complete absence of scalar diffusion ( $Pe = \infty$ ), initial concentrations are conserved along particle trajectories and (2) is equivalent to (3) through the relation

$$C(\mathbf{x}, t) = C_0(\phi^{-t}(\mathbf{x})),$$

where  $C_0$  is the initial concentration profile and  $\phi^{-t}$  is the solution of the Lagrangian equations mapping the location at time  $t$  to the particle's initial position at time 0. The zero-diffusivity limit is, however, singular and the connection between flow features and statistics derived from conservative Lagrangian dynamics and the 'persistent patterns' and variance decay rates of scalar fields in the presence of small, but non-zero diffusivity is a classic problem that continues to receive considerable attention (Pierrehumbert, 1994; Rothstein et al., 1999; Haller and Yuan, 2000; Liu and Haller, 2004).

Our interest here is narrowly focussed on the following questions:

- What tracer metrics identify the difference between mixed layer flows characterized by  $Fr = 0.1$  and  $Fr = 1.0$ ?
- What role does the scalar diffusivity play? How do tracer-based mixing metrics compare to purely Lagrangian measures?
- What is the impact of 3D motions on the tracer fields?

#### 5.2.1. Measures of tracer mixing/transport

We seek to quantify the transport and mixing of the passive tracer field during the mixed layer adjustment process using measures that are readily computable from observational data and that allow direct comparisons to any available Lagrangian observations. Moments of the distribution of the tracer field can be computed either in the horizontal at fixed depth

$$M_{mp}(t; z_0) = \frac{1}{A} \iint x^m y^p C(x, y, z_0, t) dx dy, \quad (12)$$

or by fully three dimensional volume averages

$$m_{mpq}(t) = \frac{1}{V} \iiint x^p y^q z^q C(x, y, z, t) dx dy dz. \quad (13)$$

For suitably chosen initial tracer and particle distributions, particle and tracer moment measures differ only due to the effects of finite diffusivity. Given the spatial homogeneity of the flow in the periodic direction, we are particularly interested in comparison of normalized horizontal second tracer moments in the cross-stream

$$\sigma_y^2(t, z_0) = \frac{M_{02}(t, z_0) - M_{01}^2(t, z_0)}{M_{00}(t, z_0)},$$

and the variance of the cross-stream particle distribution

$$D_y^2(t; z_0) = \langle y_i(t; z_0) - \langle y_i(t; z_0) \rangle \rangle^2.$$

Additionally, knowledge of the scalar gradient field allows one to compute a metric which directly measures the competition between advection by large-scale, presumably coherent, features in the velocity field and the diffusion acting on small scales,

$$\chi^2(t) = \frac{\int |\nabla C(\mathbf{x}, t)|^2 d\Omega}{\int |C(\mathbf{x}, t)|^2 d\Omega} = \frac{\int |\mathbf{k}|^2 |\tilde{C}(\mathbf{k}, t)|^2 d\mathbf{k}}{\int |\tilde{C}(\mathbf{k}, t)|^2 d\mathbf{k}}. \quad (14)$$

Here  $\Omega$  is either a two dimensional area at constant depth or the full, three-dimensional domain and  $\tilde{C}$  is the Fourier transform of

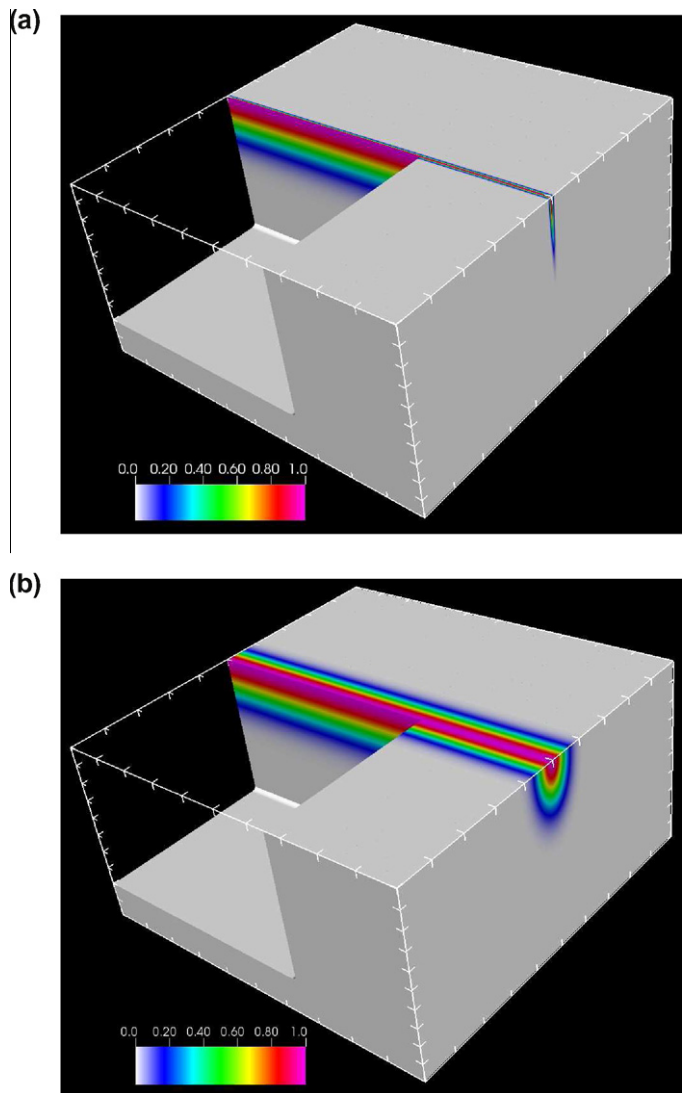


**Fig. 16.** Three-dimensional view of the initial tracer concentration field  $C$  for (a) ic1, and (b) ic2. The color bar shows non-dimensional concentration, and thick marks are placed every 1 km in the horizontal and 50 m in the vertical directions. (For interpretation of the references to color in this figure legend, the reader is referred to the web version of this article.)

the concentration with corresponding wavenumber vector  $\mathbf{k}$ . Mathematically,  $\chi^2(t)$  is the (time-dependent) Dirichlet quotient of the advection–diffusion operator. As argued in Pattanayak (2001) and Sundaram et al. (2009), saturation of  $\chi^2$  at intermediate times implies that the scalar energy and enstrophy norms decay at identical rates. Physically,  $\chi^2$  measures the mean-square radius of the scalar distribution in  $\mathbf{k}$  space, reflecting the distance between the largest stirring scales and the smallest length scales at which advection can produce structure in the presence of diffusive smoothing. Saturation of  $\chi^2$  therefore implies self-similar decay of the tracer spectrum and the existence of a ‘strange eigenmode’, with principal eigenvalue given by  $\chi^2$ , as described by Pierrehumbert (1994).

### 5.2.2. Tracer initialization

The choice of initial conditions for the tracer fields represents a trade-off between the practicalities of potential experimental designs and the finite resolution of the numerical model. For simplicity, we consider stream-wise independent initial conditions of the form:

$$C_0(\mathbf{x}) = \exp\left(-\frac{(y-y_c)^2}{\ell_y^2}\right) \exp\left(-\frac{z^2}{\ell_z^2}\right), \quad (15)$$

where  $y_c = 10,000$  m is at the center of the domain. The tracer is released in fully non-linear mixed layer flows at instances shown in Fig. 2b and d, for  $Fr = 0.1$  and  $Fr = 1.0$  cases, respectively (same in most particle experiments).

In order to determine  $\ell_y$  and  $\ell_z$ , the length scales controlling the horizontal and vertical distribution of the initial tracer patch, several practical issues require consideration. Restrictions on the total dye amount available in observational tracer deployments typically constrain initial patches to be  $\sim 50$  m wide and several meters thick (Badin et al., in press, personal communication with Miles Sundermeyer and James Ledwell, 2010). Numerically, such initial conditions imply overall patch dimensions approaching the model mesh spacing, especially in the vertical direction. As such, we conduct two experiments in parallel with initial concentrations as shown in Fig. 16. In the first case, (denoted ic1), we set  $\ell_y = 50$  m which, while approximating observational practice, is near the

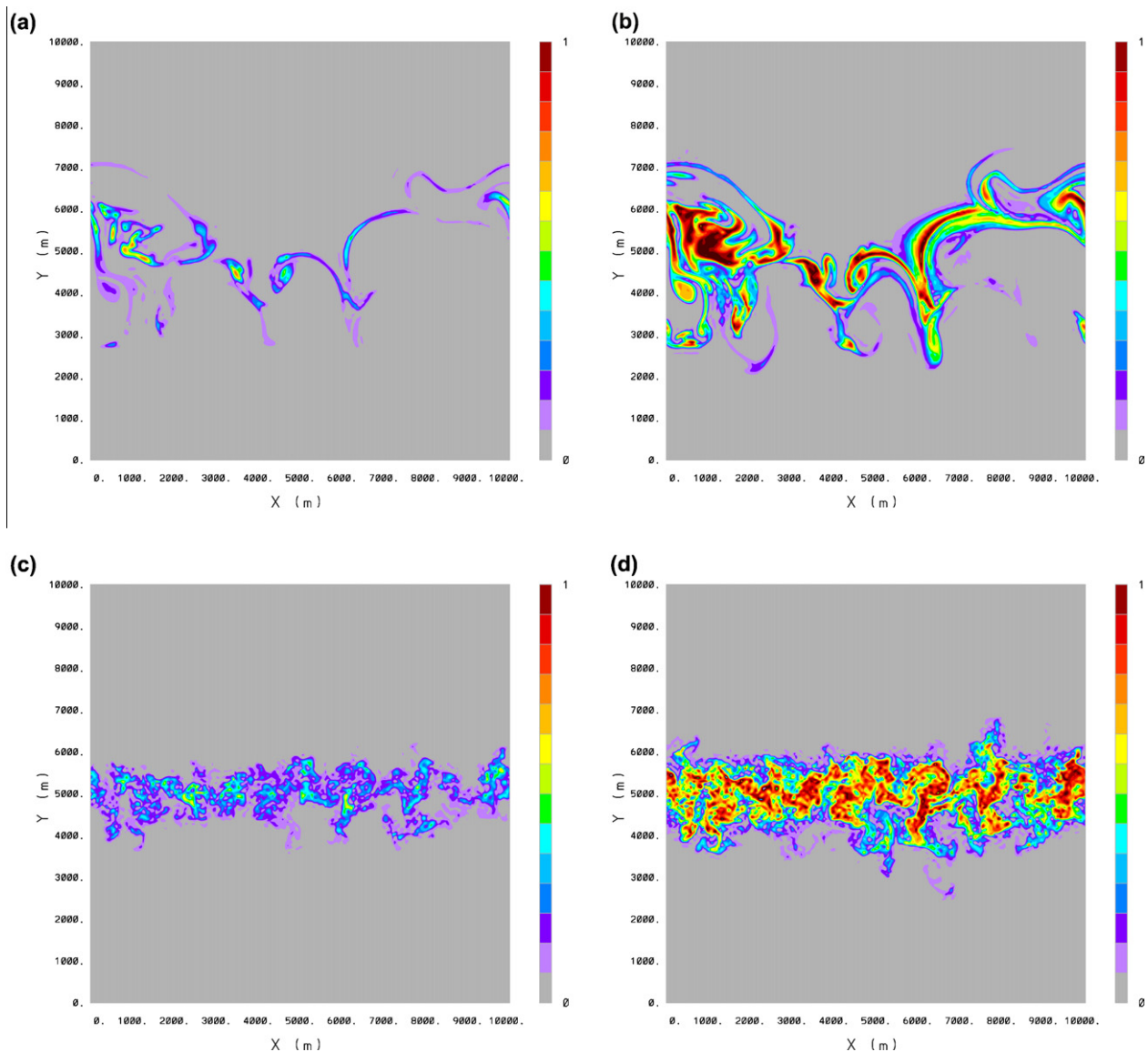


**Fig. 17.** Tracer concentration field at 5 m depth level at  $\Delta t/\tau^* = 12$ . The strongly-stratified case  $Fr = 0.1$  with (a) ic1, and (b) ic2. The weakly-stratified case  $Fr = 1.0$  with (c) ic1 and (d) ic2.

limits of horizontal model resolution. The second experiment (denoted ic2) with  $\ell_y = 500$  m is fully resolved. In both cases the vertical distribution is fixed by resolution to be  $\ell_z = 100$  m. While such a deployment may not be directly feasible in a field experiment, it allows us to investigate tracer sampling of mixed layer instabilities reliably without introducing potential numerical artifacts.

### 5.2.3. Tracer evolution in 2D

Horizontal snapshots of passive scalar evolution at 5 m depth are shown in Fig. 17 for the two different values of  $Fr$  and both initial conditions. To facilitate comparison with the previously computed Lagrangian statistics, the tracer was initialized to coincide with the particle releases shown in Fig. 9. For a fixed value of  $Fr$ , both initial conditions result in very similar patterns despite the large difference in horizontal extent and total mass of tracer released. Given the large Peclet number ( $Pe = 7 \times 10^7$ ), it is not surprising that the scalar fields closely mirror the distributions of Lagrangian particles shown in Figs. 12 and 13.

To quantify the differences in scalar evolution for different stratifications, horizontal wavenumber spectra of the near surface (5 m) tracer field are shown in Fig. 18. The spectra were computed by averaging over 56 one-dimensional spectra taken along the periodic direction for  $4 \text{ km} \leq y \leq 6 \text{ km}$  at two nondimensional times from the initial tracer release. By  $\Delta t/\tau^* = 24$ , both spectra

show approximate  $k^{-1}$  scaling in the limited inertial range. Best fit exponents were found to be  $n = 0.97$  and  $n = 0.92$  for  $Fr = 0.1$  and  $Fr = 1.0$  in the range  $0.0002 < k < 0.002$ . Such scaling is consistent with classical 2D turbulence for non-local ( $k^{-a}$ ,  $a \geq 3$ ) kinetic energy spectra (Vallis, 2006). At both times shown, however, there is a pronounced difference in the scalar spectral decay rate for the two flows at scales smaller than 0.3 km. In contrast to standard inertial-range theory, the scalar spectrum for the  $Fr = 0.1$  flow, despite its steeper kinetic energy spectra, exhibits enhanced dissipation at these scales. It is plausible that this behavior is explained by the increased levels of vertical shear present in the more strongly stratified flow resulting in much larger values of vertical diffusivity in the  $Fr = 0.1$  case (see Fig. 23).

Direct comparison of tracer and particle based mixing measures in the near surface are shown in Fig. 19. The initial particle distribution was modified slightly in order to match the initial value of  $D_y^2$  with the tracer value of  $\sigma_y^2$  given by ic2. For both  $Fr$  values, the scalar diffusivity is such that  $Pe = 7 \times 10^5$ . Independent of stratification level, there is an initial, advection dominated time period ( $t \sim 10$  turnover times) where the scalar and particle measures are identical and both grow super-diffusively. Linear, diffusive growth of both  $\sigma_y^2$  and  $D_y^2$  occurs quickly in the small scale,

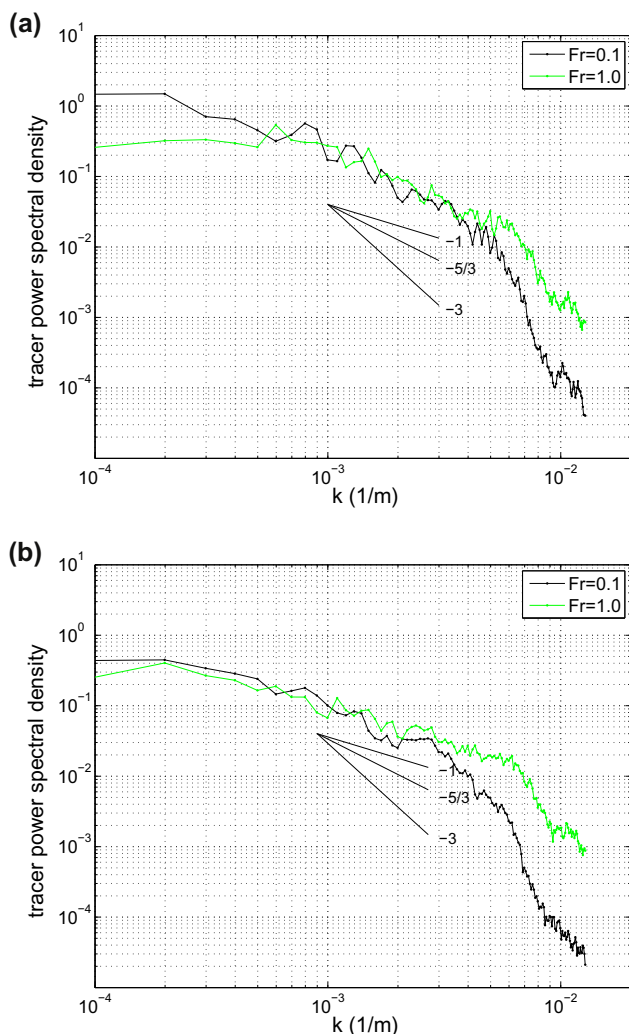


Fig. 18. Tracer wave-number power spectral density for  $Fr = 0.1$  and  $Fr = 1.0$  with ic1 at (a)  $\Delta t/\tau^* = 12$  and (b)  $\Delta t/\tau^* = 24$ .

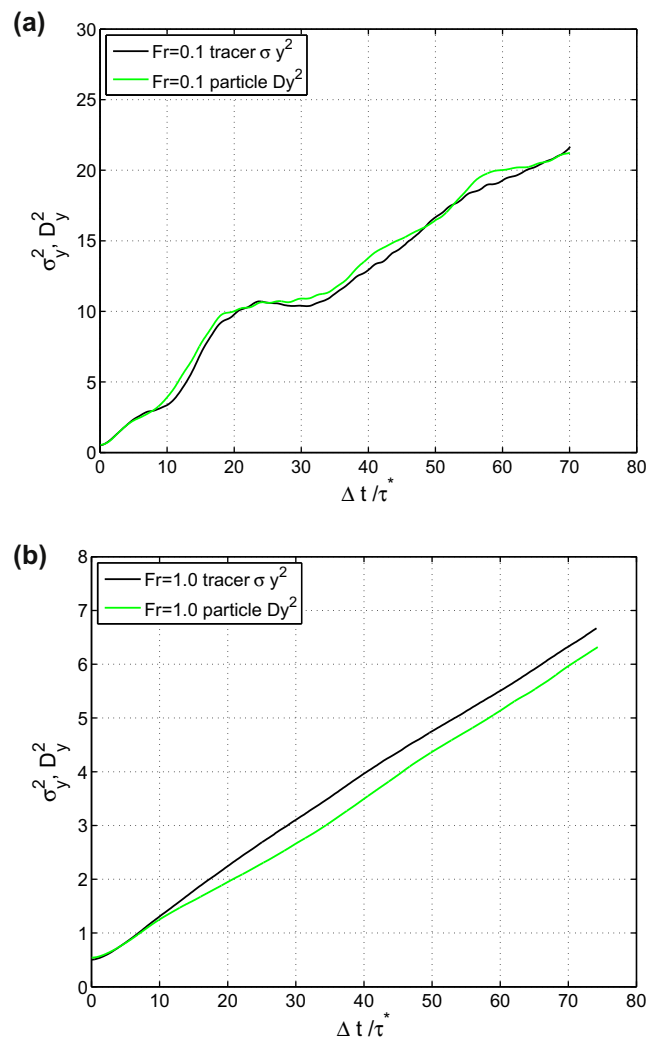


Fig. 19. Time evolution of the second moments of both tracer and particle distributions in (a) strongly stratified ( $Fr = 0.1$ ) and (b) weakly stratified ( $Fr = 1.0$ ) flows.

uncorrelated flow associated with  $Fr = 1.0$ . In the highly stratified,  $Fr = 0.1$  case where the flow is dominated by large scale coherent structures, correlations persist in both measures for considerably longer times. While there is very little difference between  $\sigma_y^2$  and  $D_y^2$  for  $Fr = 0.1$ ,  $\sigma_y^2$  is appreciably larger than  $D_y^2$  in the  $Fr = 1.0$  flow. This is consistent with the disparity between structure sizes in the two cases. For the given value of  $Pe$ , there is significant diffusive draining from the small scale vortical structures produced in the weakly stratified dynamics.

Details of the competition between horizontal tracer advection and diffusion are investigated in Fig. 20 which shows  $\chi_{2D}^2(z_0, t)$  computed from horizontal tracer fields and horizontal gradients at  $z_0 = 5$  m. The short-time evolution of  $\chi_{2D}^2(z_0, t)$  is highly dependent on the tracer initial condition. For ic1, where the initial tracer distribution is localized at scales close to the mesh spacing, diffusion immediately acts to decrease scalar gradients and  $\chi^2(t)$  decreases. In contrast, for ic2 where the tracer is initially smooth and larger scale,  $\chi^2(t)$  increases indicating scalar gradient production under the action of advection and a broadening of the spectral radius of the scalar distribution. After approximately 50 eddy turnover times, the effect of the initial conditions has essentially disappeared and the scalar field evolves towards a slowly decaying equilibrium state where scalar gradient removal by diffusive processes is nearly balanced by advective gradient production. Investigation of longer time behavior of  $\chi^2$  is limited by the finite size of the model domain. The terminal integration time,  $\Delta t/\tau^* \approx 73$ , coincides with the time when the tracer released in the  $Fr = 0.1$  flow reaches the closed boundaries which then strongly influence subsequent gradient production.

The close similarity between the  $\chi^2$  curves produced by both the  $Fr = 1.0$  and  $Fr = 0.1$  flows indicates the dominant role played by the horizontal rate of strain (or equivalently, any measure of its principal eigenvalues) in the production and maintenance of horizontal tracer gradients. This is especially apparent in the complete collapse across  $Fr$  of the initial growth of  $\chi^2(t)$  for ic2. The initial growth rate of  $\chi^2$ , for those initial conditions and  $Pe$  values producing initial growth, depends only on the Lyapunov exponent of the flow (the averaged infinitesimal stretching rate) and is independent of  $Pe$  (Sundaram et al., 2009). For tracer initial conditions for which  $\chi^2(0)$  decays, similar arguments indicate that the decay rate depends principally on the Lyapunov exponent and  $Pe$ . Since the limiting value of the Lyapunov exponent scales equally well with either the positive Okubo–Weiss parameter (Fig. 10b) or the

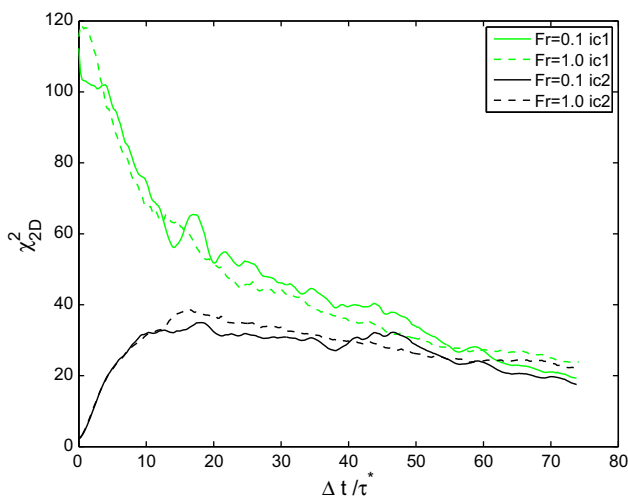


Fig. 20. Comparison of  $\chi_{2D}^2$  from 5 m passive scalar fields in strongly and weakly stratified flows for different initializations.

rms vorticity, the initial collapse of  $\chi^2$  in rescaled time for the two Froude number flows is not unexpected.

#### 5.2.4. Tracer evolution in 3D

While the results in Fig. 20 show indications that the quasi-equilibrium value of  $\chi^2$  may be lower for the  $Fr = 0.1$  flow, the time traces of  $\chi_{2D}^2$  do not clearly differentiate between the two Froude number flow regimes. As shown in Fig. 21, there are distinct differences in both the horizontal and vertical evolution of the scalar field across Froude numbers. In particular, large scale horizontal motions in the highly stratified case lead to convergence of isopycnal surfaces and the production of large vertical gradients in the scalar. This effect is much less pronounced in the  $Fr = 1.0$  flow.

Differences in vertical gradient production are clearly seen in the computation of  $\chi_{3D}^2$  shown in Fig. 22. Unlike the strictly horizontal computation, accounting for vertical gradient production clearly indicates that  $\chi_{3D}^2$  grows more rapidly and equilibrates at a significantly larger value in the more energetic, highly stratified flow. Also in contrast to the slow decay of  $\chi_{2D}^2$  seen in Fig. 20,  $\chi_{3D}^2$  approaches a nearly constant value in all cases indicating that the self similar decay of the tracer spectrum previously observed in simple 2D periodic flows and maps persists in the complex, aperiodic mixed layer adjustment process. Investigation of the dependence of  $\chi_{3D}^2$  on the value of the diffusivity indicates that while the equilibrium value is set by  $Pe$ , the initial growth is  $Pe$  independent as argued above.

To connect the behavior of the tracer based metric to Lagrangian particle measures, we seeded the flow fields with a 3D distribution of synthetic drifters and computed the evolution of the vertical particle variance. The results, shown in Fig. 23, are consistent with the tracer observations. Rough estimates of the vertical eddy diffusivity indicate that this quantity is approximately one order of magnitude larger in the more stratified flow field. For  $Fr = 0.1$ , particle distributions initially centered at 50 m depth

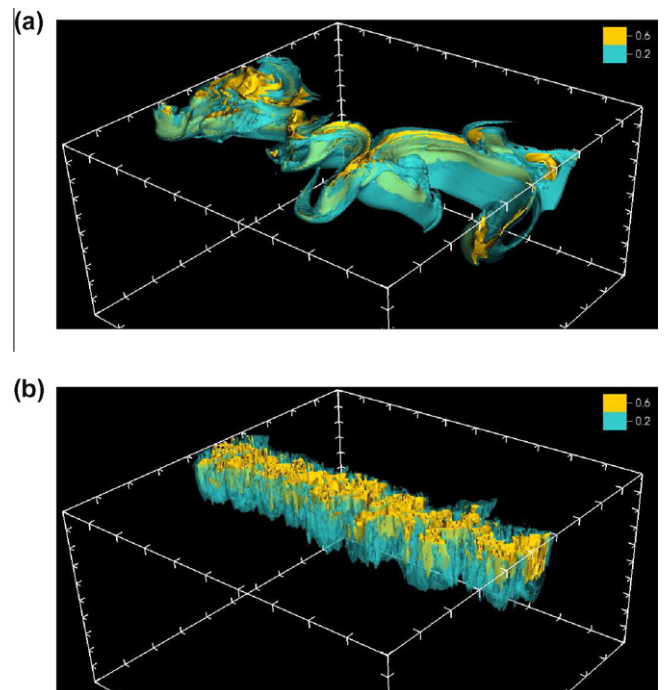


Fig. 21. Contours of the tracer concentration values of  $C = 0.2$  (blue) and  $C = 0.6$  (yellow) starting with initial condition ic2 at  $\Delta t/\tau^* = 12$  for (a) the strongly-stratified case  $Fr = 0.1$ , and (b) the weakly-stratified case  $Fr = 1.0$ . The thick marks are placed every 1 km in the horizontal and 50 m in the vertical directions. (For interpretation of the references to color in this figure legend, the reader is referred to the web version of this article.)

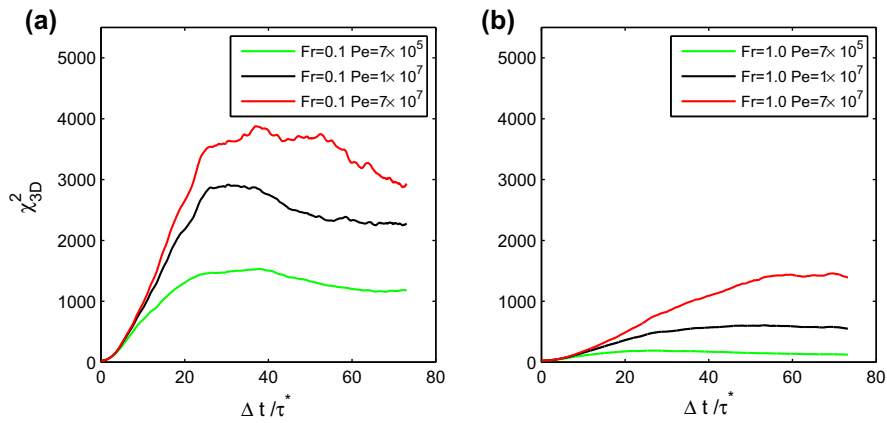


Fig. 22. Comparison of domain-averaged  $\chi_{3D}^2$  from passive scalar fields in (a) strongly stratified ( $Fr = 0.1$ ) and (b) weakly stratified ( $Fr = 1.0$ ) flows for ic2 initial condition and three values of the scalar diffusivity.

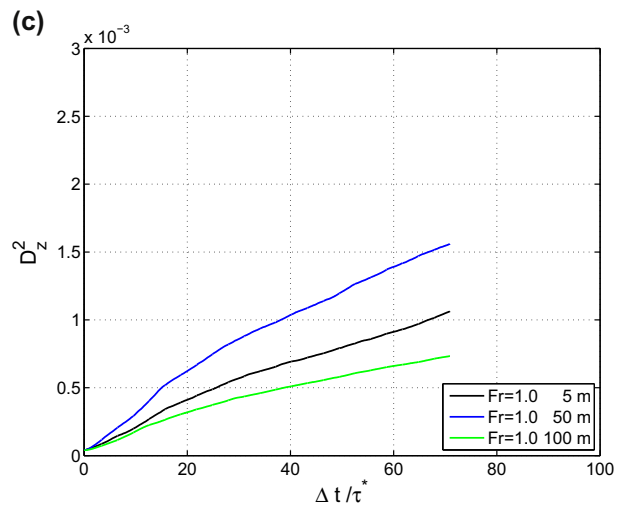
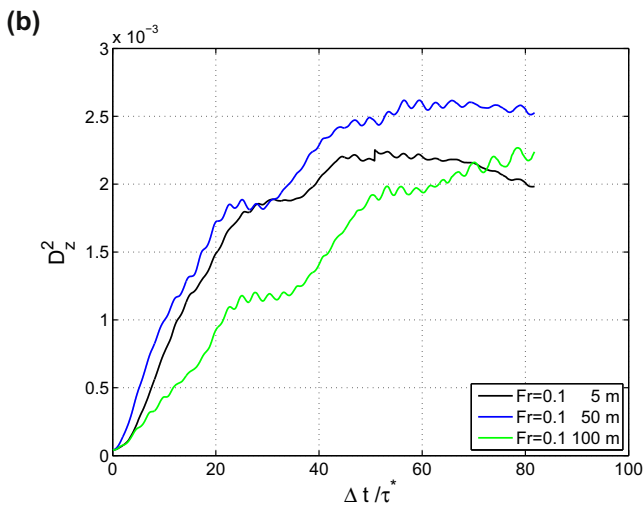
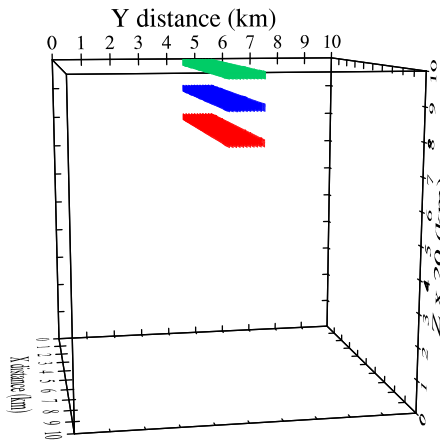


Fig. 23. Lagrangian calculation of vertical diffusivity. (a) Initial, 3D, distribution of particles centered at three levels of 5 m ( $10\text{ m} \geq z \geq 0$  m with  $\Delta z = 1$  m), 50 m ( $55\text{ m} \geq z \geq 45$  m with  $\Delta z = 1$  m) and 100 m ( $105\text{ m} \geq z \geq 95$  m with  $\Delta z = 1$  m); while the horizontal same area as in previous sampling is maintained using  $11 \times 91$  particles with  $\Delta x \Delta y = 100$  m. A total of  $11 \times 91 \times 11 \times 3 = 33,033$  particles are released. Time evolution of second moment in  $z$ ,  $D_z^2(t; z_0) = \langle z_i(t; z_0) - \langle z_i(t; z_0) \rangle \rangle^2$ , for (b)  $Fr = 0.1$  and (c)  $Fr = 1.0$  flows.

evolve vertically so that encounters with the free surface begin to corrupt the statistics around 40 eddy turnover times. In contrast, the vertical variance of the particle distributions at all depth levels

in the  $Fr = 1.0$  flow show clear indications of linear growth throughout the integration time and remain, on average, well below the free surface.

## 6. Summary and conclusions

In light of the recognition of the role played by submesoscale processes as a fundamental part of the ocean's energy cascade, as well as their potential importance for both horizontal and vertical biogeochemical transport, LES of isolated mixed layer instabilities, a particular class of submesoscale flows, are conducted. The primary objective behind these simulations is to generate velocity and density fields representative of rapidly-evolving submesoscale flows with spatial scales on the order of 100 m to 10 km to allow testing of sampling strategies.

Mixed layer instabilities are explored in two parameter regimes. The strongly-stratified,  $Fr = 0.1$ , regime clearly exhibits surface-intensified eddies with scales of approximately 2 km and high vertical shears across the mixed layer. The weakly-stratified,  $Fr = 1.0$ , regime has weak eddies of 0.2 km scale that penetrate across the entire depth of the domain as Taylor columns. Kinetic energy spectra indicate a forward enstrophy scaling of  $k^{-3}$  for the  $Fr = 0.1$  case while the  $Fr = 1.0$  case shows indications of both a  $k^{-5/3}$  backward energy cascade and  $k^{-3}$  forward enstrophy cascade transitioning approximately at the scale of the submesoscale eddies.

Two sampling methods are tested. First, Lagrangian particles are released near the surface, the middle of the mixed layer and near the mixed layer base in order to compute dispersion statistics in the system. In both flow regimes, distributions of Finite Scale Lyapunov Exponents reveal a Richardson regime for separation scales larger than the submesoscale eddy size and an exponential scaling at smaller separation distances. The size of the peak Lyapunov exponents is shown to scale very well with the average hyperbolicity, Okubo–Weiss partition consistent with recent modeling studies (Poje et al., 2010). The velocity fields are highly anisotropic due to the large aspect ratio of the domain and horizontal strain dominates vertical strain. As such, no significant differences are found in the statistics of particles advected with either horizontal or fully 3D velocity fields provided the particles are initially launched at constant depth levels. It is shown that fairly unbiased estimates of the scale-dependent FSLE curves can be obtained within an uncertainty factor of two on the basis of only nine triplets. This appears to be a very encouraging result pointing towards an economical sampling of relative dispersion for submesoscale processes using Lagrangian instruments.

Given the range of scales, computation of the details of turbulent coherent structures using Lagrangian methods is prohibitively expensive requiring the use of  $O(10^5)$  particles. As such, the use of a passive tracer, which also follows the fluid motion (but is not fully Lagrangian, in the strict mathematical sense), is explored. A particular motivation for doing so is given by recent developments in sampling technologies that may enable 3D synoptic scanning of near-surface dye in the ocean.

Tracer fields evolving under advective–diffusive dynamics are analyzed in several stages. For both Froude number regimes, horizontal tracer wavenumber spectra at 5 m depth show approximate inertial range  $k^{-1}$  scaling consistent with a non-local, 2D turbulence. There is, however, a distinct difference in the tracer spectra at smaller scales where the  $Fr = 0.1$  case exhibits much faster decay. The enhanced tracer dissipation at the smaller scales is consistent with an order of magnitude larger vertical particle diffusivity found for  $Fr = 0.1$  compared to  $Fr = 1.0$ .

The competition between the sharpening of the tracer gradients by coherent features in the velocity field, and diffusion acting on small scales is investigated by computing the Dirichlet quotient or average spectral radius of the tracer field. When only horizontal gradients are considered, this metric ( $\chi_{2D}$ ) shows that the effect of the tracer initial conditions disappears after approximately 50 eddy turnover times and scalar distributions evolve towards a qua-

si self-similar state where scalar gradient removal by diffusion is nearly balanced by advective gradient production. The scaled time evolution of  $\chi_{2D}$ , like the behavior of the inertial range horizontal scalar spectra, is found to be very similar in both Froude number regimes. In contrast, when vertical gradients are included,  $\chi_{3D}$  is found to grow much faster and achieve a much larger equilibrium value in the more strongly stratified,  $Fr = 0.1$ , flow.

The implications of this very idealized setting concerning dispersion studies using floats and dye deserve a discussion. Typical open ocean conditions include wind, wave and buoyancy forcing. None of these factors is included here. For instance, it is known that wind forcing can exert a strong influence on the dynamics of fronts, such as formation of vertical circulations and multiple fronts within a baroclinic zone, depending on the wind direction (as discussed by Thomas and Lee (2005)). Another process that is known to be important at the ocean's surface at such scales is the Langmuir circulation (Langmuir, 1938), which tends to create bands of convergence/divergence zones that are typically 2–300 m apart and some 10 times greater in length with vertical velocities reaching as high as 25 cm/s (Weller and Price, 1988). Langmuir cells arise from the interaction between the Stokes drift due to surface waves and the vertical shear of the wind-induced currents (Craig and Leibovich, 1976). Large eddy simulations of this process reveal very complex patterns (Skylingstad and Denbo, 1995). As such, it is very likely that dispersion of both dye and floats will be influenced by near-surface forcing. For instance, features resembling Langmuir cells have been detected using a coastal VHF radar and these appear to exert a strong influence on observed drifter trajectories (Haza et al., 2010). Nevertheless, since these features are at best marginally resolved by VHF radars, the investigation of this question is still at the frontiers of research.

In terms of practical insight gained from these computations for use in observational programs, we can propose an adaptive strategy consisting of an hybrid sampling method, highlighting strengths of each sampling technique in an attempt to optimize the resources. Given that little would be known about the fine details of the underlying flow field, the first step could consist of sampling with long strips of passive tracers and identifying fastest-growing branches of the tracer field using airborne lidar. These branches are likely to be associated with exponential stretching in the hyperbolic regions that would be responsible for the generation of submesoscale filaments, and pinpoint the relatively narrow regions in the flow field at which further sampling should be directed. The second stage would be to seed these fastest-growing branches with as many Lagrangian drifters as resources allow, as well as placing some drifters in the intermediate space, in order to obtain accurate velocity measurements. In addition, other instruments such as gliders can be targeted using this approximate of the flow topology in order to take vertical profiles. This can then allow computation of some of the components of the velocity gradient tensor with modest resources with respect to the degrees of freedom in the flow field. As it is based on Lagrangian platforms, a sampling strategy of this sort should work better than fixed-grid approaches for rapidly-deforming submesoscale fields.

Future studies of submesoscale processes will be aimed at capturing the impact of mesoscale structures either in modeled or truly resolved multi-scale computations.

## Acknowledgments

We greatly acknowledge the support of the Office of Naval Research and National Science Foundation via Grants N00014-09-1-0267, DMS-1025323, DMS-1025359 under the Collaborative Mathematics and Geoscience (CMG) initiative. We thank all members of the Lateral Mixing DRI team, who have provided guidance

through many insightful comments. The authors also thank the two anonymous reviewers whose constructive comments led to a significant improvement of this manuscript. Most computations were carried out on the University of Miami's high-performance computing (HPC) center (<http://ccs.miami.edu/hpc/>). The authors thank the center's director Nicholas Tsinoremas, HPC director Joel Zysman for these resources and convenient access, and especially Zongjun Hu for his continuous daily assistance and help. A significant and important portion of the computations were completed on SystemX at Virginia Tech's advanced research computing center (<http://www.arc.vt.edu>). We thank Dr. Terry Herdman and Michael Snow for their help. The generous help provided by Hank Childs on his visualization software visit has been critical for the graphics in this manuscript.

## References

- Artale, V., Boffetta, G., Celani, A., Cencini, M., Vulpiani, A., 1997. Dispersion of passive tracers in closed basins: beyond the diffusion coefficient. *Phys. Fluids* 9, 3162–3171.
- Aurell, E., Boffetta, G., Crisanti, A., Paladin, G., Vulpiani, A., 1997. Predictability in the large: an extension of the concept of Lyapunov exponent. *J. Phys. A* 30, 1–26.
- Badin, G., Tandon, A., Mahadevan, A., in press. Lateral mixing in the pycnocline by baroclinic mixed layer eddies. *J. Phys. Oceanogr.*
- Bennett, A.F., 1984. Relative dispersion – local and nonlocal dynamics. *J. Atmos. Sci.* 41 (11), 1881–1886.
- Berloff, P., McWilliams, J., 2002. Material transport in oceanic gyres. Part 2: Hierarchy of stochastic models. *J. Phys. Oceanogr.* 32 (3), 797–830.
- Boccaletti, G., Ferrari, R., Fox-Kemper, B., 2007. Mixed layer instabilities and restratification. *J. Phys. Oceanogr.* 37, 2228–2250.
- Capet, X., McWilliams, J., Molemaker, M., Shchepetkin, A., 2008. Mesoscale to submesoscale transition in the California Current System: I. Flow structure, eddy flux and observational tests. *J. Phys. Oceanogr.* 38, 29–43.
- Chang, Y., Xu, X., Özgökmen, T., Chassignet, E., Peters, H., Fischer, P., 2005. Comparison of gravity current parameterizations and calibration using a high-resolution 3d nonhydrostatic spectral element model. *Ocean Modell.* 10, 342–368.
- Chassignet, E., Hurlburt, H., Smedstad, O., Halliwell, G., Hogan, P., Wallcraft, A., Bleck, R., 2006. Ocean prediction with the Hybrid Coordinate Ocean Model (HYCOM). *Ocean Weather Forecast.* 5, 413–426.
- Coulliette, C., Wiggins, S., 2000. Intergyre transport in a wind-driven, quasigeostrophic double gyre: an application of lobe dynamics. *Nonlinear Process. Geophys.* 7, 59–85.
- Craik, A., Leibovich, S., 1976. A rational model for Langmuir circulations. *J. Fluid Mech.* 73, 401–426.
- D'Asaro, E.A., 2003. Performance of autonomous Lagrangian floats. *J. Atmos. Oceanic Technol.* 20, 896–911.
- D'Asaro, E., Farmer, D., Osse, J., Dairiki, G., 1996. A Lagrangian float. *J. Atmos. Oceanic Technol.* 13, 1230–1246.
- Davis, R., 1991. Observing the general-circulation with floats. *Deep-Sea Res.* 38, 531–571.
- d'Ovidio, F., Fernandez, V., Hernandez-Garcia, E., Lopez, C., 2004. Mixing structures in the Mediterranean sea from finite-size Lyapunov exponents. *Geophys. Res. Lett.* 31, L17203. doi:10.1029/2004GL020328.
- Eldevik, T., Dysthe, K., 2002. Spiral eddies. *J. Phys. Oceanogr.* 32, 851–869.
- Falco, P., Griffa, A., Poulain, P., Zambianchi, E., 2000. Transport properties in the adriatic sea as deduced from drifter data. *J. Phys. Oceanogr.* 30, 2055–2071.
- Fischer, P.F., 1997. An overlapping Schwarz method for spectral element solution of the incompressible Navier–Stokes equations. *J. Comput. Phys.* 133, 84–101.
- Fox-Kemper, B., Ferrari, R., Hallberg, R., 2008. Parameterization of mixed-layer eddies. Part I: Theory and diagnosis. *J. Phys. Oceanogr.* 38, 1145–1165.
- Fratantoni, D., 2001. North Atlantic surface circulation during the 1990's observed with satellite-tracked drifters. *J. Geophys. Res.* 106, 22067–22093.
- Griffa, A., 1996. Applications of stochastic particle models to oceanographic problems. In: Adler, R., Müller, P., Rozovskii, B. (Eds.), *Stochastic Modelling in Physical Oceanography*, vol. 467. Birkhauser, Boston, pp. 113–128.
- Haller, G., 1997. Distinguished material surfaces and coherent structures in three-dimensional flows. *Physica D* 149 (4), 248–277.
- Haller, G., Poje, A., 1998. Finite time transport in aperiodic flows. *Physica D* 119, 352–380.
- Haller, G., Yuan, G., 2000. Lagrangian coherent structures and mixing in two-dimensional turbulence. *Physica D* 147, 352–370.
- Haza, A.C., Griffa, A., Martin, P., Molcard, A., Özgökmen, T.M., Poje, A.C., Barbanti, R., Book, J.W., Poulain, P.M., Rixen, M., Zanasca, P., 2007. Model-based directed drifter launches in the Adriatic Sea: results from the DART experiment. *Geophys. Res. Lett.* 34. doi:10.1029/2007GL029634.
- Haza, A.C., Poje, A., Özgökmen, T.M., Martin, P., 2008. Relative dispersion from a high-resolution coastal model of the Adriatic Sea. *Ocean Modell.* 22, 48–65.
- Haza, A., Özgökmen, T., Griffa, A., Molcard, A., Poulain, P., Peggion, G., 2010. Transport properties in small scale coastal flows: relative dispersion from VHF radar measurements in the Gulf of La Spezia. *Ocean Dyn.* 60, 861–882.
- Ilicak, M., Özgökmen, T., Özsoy, E., Fischer, P., 2009. Non-hydrostatic modeling of exchange flows across complex geometries. *Ocean Modell.* 29, 159–175.
- Kaplan, D., Largier, J., Botsford, L., 2005. HF radar observations of surface circulation off Bodega Bay (northern California, USA). *J. Geophys. Res.* 110. doi:10.1029/2005JC002959.
- Klein, P., Lapeyre, G., 2009. The oceanic vertical pump induced by mesoscale and submesoscale turbulence. *Annu. Rev. Mar. Sci.* 1, 351–375.
- Koszalka, I., LaCasce, J.H., Orvik, K.A., 2009. Relative dispersion statistics in the Nordic Seas. *J. Mar. Res.* 67, 411–433.
- LaCasce, J.H., 2008. Statistics from Lagrangian observations. *Prog. Ocean.* 77 (1), 1–29.
- LaCasce, J.H., Ohlmann, C., 2003. Relative dispersion at the surface of the Gulf of Mexico. *J. Mar. Res.* 61 (3), 285–312.
- Lacorata, G., Aurell, E., Vulpiani, A., 2001. Drifter dispersion in the Adriatic sea: Lagrangian data and chaotic model. *Ann. Geophys.* 19, 121–129.
- Langmuir, I., 1938. Surface motion of water induced by wind. *Science* 41, 119–123.
- Ledwell, J., Watson, A.J., Law, C., 1998. Mixing of a tracer in the pycnocline. *J. Geophys. Res.* 103, 21499–21529.
- Lee, C.M., D'Asaro, E.A., Harcourt, R., Rainville, L. An integrated modeling and observational study of three-dimensional upper ocean boundary layer dynamics and parameterizations: a brief progress report. Unpublished report, 13 p.
- Liu, W., Haller, G., 2004. Strange eigenmodes and decay of variance in the mixing of diffusive tracers. *Physica D* 188, 1–39.
- Lumpkin, R., Elipot, S., 2010. Surface drifter pair spreading in the North Atlantic. *J. Geophys. Res. – Oceans* 115, C12017.
- Lumpkin, R., Pazos, M., 2007. Measuring surface currents with Surface Velocity Program drifters: the instrument, its data, and some recent results. In: Griffa, A., Kirwan, A.D., Mariano, A., Özgökmen, T., Rossby, T. (Eds.), *Lagrangian Analysis and Prediction of Coastal and Ocean Dynamics*, pp. 39–67.
- Maday, Y., Patera, A.T., 1989. Spectral element methods for the Navier–Stokes equations. In: Noor, A.K. (Ed.), *State of the Art Surveys in Computational Mechanics*. ASME, pp. 71–143.
- Mahadevan, A., 2006. Modeling vertical motion at ocean fronts: are nonhydrostatic effects relevant at submesoscales? *Ocean Modell.* 14, 222–240.
- Mahadevan, A., Tandon, A., 2006. An analysis of mechanisms for submesoscale vertical motion at ocean fronts. *Ocean Modell.* 14, 241–256.
- Mahadevan, A., Tandon, A., Ferrari, R., 2010. Rapid changes in the mixed layer stratification driven by submesoscale instabilities and winds. *J. Geophys. Res.* 115 (C03017). doi:10.1029/2008JC005203.
- Martin, P., Book, J., Burrage, D., Rowley, C., Tudor, M., 2009. Comparison of model-simulated and observed currents in the central Adriatic during DART. *J. Geophys. Res.* 114. doi:10.1029/2008JC004842.
- McWilliams, J.C., 1985. Submesoscale, coherent vortices in the ocean. *Rev. Geophys.* 23 (2), 165–182.
- McWilliams, J., 2008. Fluid dynamics at the margin of rotational control. *Environ. Fluid Mech.* 8, 441–449.
- Miller, P., Pratt, L., Helfrich, K., Jones, C., 2002. Chaotic transport of mass and potential vorticity for an island recirculation. *J. Phys. Oceanogr.* 32, 80–102.
- Molcard, A., Poje, A., Özgökmen, T., 2006. Directed drifter launch strategies for lagrangian data assimilation using hyperbolic trajectories. *Ocean Modell.* 12, 268–289.
- Müller, P., McWilliams, J., Molemaker, M., 2005. Routes to dissipation in the ocean: the two-dimensional/three-dimensional turbulence conundrum. In: Baumert, H.Z., Simpson, J., Sündermann, J. (Eds.), *Marine Turbulence: Theories, Observations, and Models*. Results of the CARTUM Project. Cambridge University Press, pp. 397–405.
- Okubo, A., 1970. Horizontal dispersion of floatable particles in vicinity of velocity singularities such as convergences. *Deep-Sea Res.* 17 (3), 445–454.
- Olascoaga, M., Rypina, I.I., Brown, M.G., Beron-Vera, F.J., Kocak, H., Brand, L.E., Halliwell, G.R., Shay, L.K., 2006. Persistent transport barrier on the West Florida Shelf. *Geophys. Res. Lett.* 33, 22603. doi:10.1029/2006GL027800.
- Ottino, J., 1989. *The Kinematics of Mixing: Stretching, Chaos and Transport*. Cambridge University Press.
- Özgökmen, T., Fischer, P., 2008. On the role of bottom roughness in overflows. *Ocean Modell.* 20, 336–361.
- Özgökmen, T.M., Fischer, P.F., Duan, J., Iliescu, T., 2004a. Three-dimensional turbulent bottom density currents from a high-order nonhydrostatic spectral element model. *J. Phys. Oceanogr.* 34 (9), 2006–2026.
- Özgökmen, T.M., Fischer, P.F., Duan, J., Iliescu, T., 2004b. Entrainment in bottom gravity currents over complex topography from three-dimensional nonhydrostatic simulations. *Geophys. Res. Lett.* 31 (L13212). doi:10.1029/2004GL020186.
- Özgökmen, T., Fischer, P., Johns, W., 2006. Product water mass formation by turbulent density currents from a high-order nonhydrostatic spectral element model. *Ocean Modell.* 12, 237–267.
- Özgökmen, T., Iliescu, T., Fischer, P., Srinivasan, A., Duan, J., 2007. Large eddy simulation of stratified mixing in two-dimensional dam-break problem in a rectangular enclosed domain. *Ocean Modell.* 16, 106–140.
- Özgökmen, T., Iliescu, T., Fischer, P., 2009a. Large eddy simulation of stratified mixing in a three-dimensional lock-exchange system. *Ocean Modell.* 26, 134–155.
- Özgökmen, T., Iliescu, T., Fischer, P., 2009b. Reynolds number dependence of mixing in a lock-exchange system from direct numerical and large eddy simulations. *Ocean Modell.* 30, 190–206.
- Paduan, J., Rosenfeld, L., 1996. Remotely sensed surface currents in Monterey Bay from shore based HF radar (Coastal Ocean Dynamics Application Radar). *J. Geophys. Res.* 101 (C9), 20669–20686.

- Paduan, J., Kim, K., Cook, M., Chavez, F., 2006. Calibration and validation of direction finding high frequency radar ocean current observations. *IEEE J. Oceanic Eng.*, 862–875. doi:10.1109/OE.2006.886195.
- Patera, A., 1984. A spectral element method for fluid dynamics; laminar flow in a channel expansion. *J. Comput. Phys.* 54, 468–488.
- Pattanayak, A., 2001. Characterizing the metastable balance between chaos and diffusion. *Physica D* 148, 1–19.
- Pierrehumbert, R., 1994. Tracer microstructure in the large-eddy dominated regime. *Chaos Solitons Fract.* 4, 1091–1110.
- Poje, A., Haller, G., 1999. Geometry of cross-stream mixing in a double-gyre ocean model. *J. Phys. Oceanogr.* 29, 1649–1665.
- Poje, A.C., Toner, M., Kirwan, A.D., Jones, C.K.R.T., 2002. Drifter launch strategies based on Lagrangian templates. *J. Phys. Oceanogr.* 32, 1855–1869.
- Poje, A., Haza, A., Özgökmen, T., Magaldi, M., Garraffo, Z., 2010. Resolution dependent relative dispersion statistics in a hierarchy of ocean models. *Ocean Modell.* 31, 36–50.
- Poulain, P.-M., 1999. Drifter observations of surface circulation in the Adriatic Sea between December 1994 and March 1996. *J. Mar. Syst.* 20, 231–253.
- Rosby, T., 2007. Evolution of lagrangian methods in Oceanography. In: Griffa, A., Kirwan, A.D., Mariano, A., Özgökmen, T., Rossby, T. (Eds.), *Lagrangian Analysis and Prediction of Coastal and Ocean Dynamics*, pp. 1–38.
- Rothstein, D., Henry, E., Gollup, J., 1999. Persistent patterns in transient chaotic fluid mixing. *Nature* 401, 770–772.
- Sagaut, P., 2006. *Large Eddy Simulation for Incompressible Flows*. Scientific Computation. Springer-Verlag, Berlin.
- Sawford, B., 2001. Turbulent relative dispersion. *Annu. Rev. Fluid Mech.* 33, 289–317.
- Schroeder, K., Haza, A.C., Griffa, A., Özgökmen, T.M., Poulain, P., Gerin, R., Peggion, G., Rixen, M., 2011. Relative dispersion in the liguro-provencal basin: from sub-mesoscale to mesoscale. *Deep-Sea Res. I* 58, 861–882.
- Shadden, S., Lekien, F., Paduan, J.D., Chavez, F.C., Marsden, J.E., 2008. The correlation between surface drifters and coherent structures based on high-frequency data in Monterey Bay. *Deep-Sea Res. II* 56, 161–172.
- Shay, L., Lentz, S., Graber, H., Haus, B., 1998a. Current structure variations detected by high frequency radar and vector measuring current meters. *J. Atmos. Oceanic Technol.* 15, 237–256.
- Shay, L., Cook, T., Hallock, Z., Haus, B., Graber, H., Martinez, J., 2001. The strength of the M2 tide at the Chesapeake Bay mouth. *J. Phys. Oceanogr.* 31, 427–449.
- Shay, L., Martinez-Pedraja, J., Cook, T., Haus, B., 2007. High-frequency radar mapping of surface currents using WERA. *J. Atmos. Oceanic Technol.* 24, 484–503.
- Skyllingstad, E.D., Denbo, D., 1995. An ocean large-eddy simulation of Langmuir circulations and convection in the surface mixed layer. *J. Geophys. Res.* 100, 8501–8522.
- Steward, R., Joy, J., 1974. HF radio measurements of surface currents. *Deep-Sea Res.* 21, 1039–1049.
- Sundaram, B., Poje, A., Pattanayak, A., 2009. Persistent patterns and multifractality in fluid mixing. *Phys. Rev. E* 79, 066202.
- Sundermeyer, M., Ledwell, J., 2001. Lateral dispersion over the continental shelf: analysis of dye release experiments. *J. Geophys. Res.* 106, 9603–9621.
- Sundermeyer, M., Terrya, E., Ledwell, J., A.G. C., LaRocque, P., Banic, J., 2007. Three-dimensional mapping of fluorescent dye using a scanning, depth-resolving airborne radar. *J. Atmos. Ocean. Technol.* 24, 1050–1065.
- Tandon, A., Garrett, C., 1994. Mixed layer restratification due to horizontal density gradients. *J. Phys. Oceanogr.* 24, 1419–1424.
- Thomas, L., Lee, C.M., 2005. Intensification of ocean fronts by down-front winds. *J. Phys. Oceanogr.* 35, 1086–1102.
- Thomas, L., Tandon, A., Mahadevan, A., 2008. Submesoscale processes and dynamics. In: Hecht, M., Hasume, H. (Eds.), *Ocean Modeling in an Eddying Regime*, Geophysical Monograph, vol. 177, pp. 17–38.
- Tseng, Y., Ferziger, J., 2001. Mixing and available potential energy in stratified flows. *Phys. Fluids* 13, 1281–1293.
- Vallis, G., 2006. *Atmospheric and Oceanic Fluid Dynamics*. Cambridge University Press, pp. 350–370.
- Veneziani, M., Griffa, A., Reynolds, A., Garraffo, Z., Chassignet, E., 2005. Parameterizations of Lagrangian spin statistics and particle dispersion in the presence of coherent vortices. *J. Mar. Res.* 63 (6), 1057–1083.
- Webb, D., Simonetti, P., Jones, C., 2001. SLOCUM: an underwater glider propelled by environmental energy. *IEEE J. Oceanic Eng.* 26, 447–452.
- Weiss, J., 1991. The dynamics of enstrophy transfer in 2-dimensional hydrodynamics. *Physica D* 48 (2–3), 273–294.
- Weller, R., Price, J., 1988. Langmuir circulation within the oceanic mixed layer. *Deep-Sea Res.* 35, 711–747.
- Wiggins, S., 2005. The dynamical systems approach to Lagrangian transport in oceanic flows. *Annu. Rev. Fluid Mech.* 37, 295–328.
- Winters, K.B., Lombard, P.N., Riley, J.J., D'Asaro, E.A., 1995. Available potential energy and mixing in density-stratified fluids. *J. Fluid Mech.* 289, 115–128.
- Wunsch, C., Ferrari, R., 2004. Vertical mixing, energy, and the general circulation of the oceans. *Annu. Rev. Fluid Mech.* 36, 281–314.
- Xu, X., Chang, Y., Peters, H., Özgökmen, T., Chassignet, E., 2006. Parameterization of gravity current entrainment for ocean circulation models using a high-order 3d nonhydrostatic spectral element model. *Ocean Modell.* 14, 19–44.